Alma Mater Studiorum – Università di Bologna

DOTTORATO DI RICERCA IN

SCIENZE CHIMICHE - Ciclo XXV°

Settore Concorsuale di afferenza: 03/A2 – Modelli e Metodologie per le Scienze Chimiche

Settore Scientifico disciplinare: CHIM/02 – Chimica Fisica

TITOLO TESI:

EXCITONIC PROCESSES IN MULTIFUNCTIONAL ORGANIC SEMICONDUCTORS FOR APPLICATION IN ORGANIC LIGHT-EMITTING TRANSISTOR

Presentata da: Stefano Troisi

Coordinatore Dottorato   Relatore:

Prof. Adriana Bigi   Prof.   Giorgio   Orlandi
                                                                      Correlatore:

                                                            Dott. Michele Muccini

Esame finale anno 2013

Contents

Introduction

In the past few decades, π-conjugated organic materials have attracted considerable attention in view of their increasing use as active elements in electronic and optoelectronic devices such as light-emitting diodes, photovoltaic cells, and field effect transistors[1,2]. Prototype systems of devices making use of organic materials are currently available, and the focus now is on improving device performances. The active semiconducting materials can be divided into two broad classes: π-conjugated molecular systems[3,4] which present precisely defined structures, and π-conjugated polymers[5], which are composed by repeating units and described by molecular weight distributions.

To achieve the maximum performance output from these devices, challenges arise from considerations that reach beyond the molecular chemical formula[6]. For isolated molecules, guidelines exist that rely on the molecular formula to tailor the frontier (HOMO-LUMO) molecular orbital energy levels and optical absorption profiles. Much less control can be achieved over relevant properties, that determine the features in the solid state. An important issue in organic electronic and photonics research is to understand the transition from simple conjugated building blocks to extended semiconducting molecules with predictable properties, and ultimately to the collective behavior of multiple components in functional devices[7].

In this direction, Organic Light-Emitting Transistors (OLETs) can be considered as a powerful platform for investigating the intimate correlation between solid-state molecular arrangement and functional properties in organics. OLETs are an innovative class of multifunctional devices in which the fundamental optical and electronic processes (such as charge transport, exciton formation, energy/charge transfer, charge trapping, etc.) are strictly connected to the active materials deposited as thin-film. It is well-known that in organic field-effect transistors, charge carrier mobility has a length scale dependence and only the first two molecular layers next to the dielectric interface contribute to the charge transport. Thus, device optoelectronic performance are mainly governed by the organic semiconductor aggregation and morphological features at the interface with the dielectric layer. As a consequence the molecular arrangement is extremely sensitive to the deposition procedures and to the nature of the substrate[8], thus it is possible to modulate the film morphologies playing with these parameters. Moreover, many studies have

shown how the degree of molecular order in organic thin film affects the optical[9] and electrical[10] properties.

In this thesis, I report on a comprehensive study about the photo-physical properties both in solution and in solid-state of a new thiophene based material *(2,2'-(2,2'-bithiophene-5,5'-diyl)bis(5-butyl-5H-thieno[2,3-c]pyrrole-4,6)-dione* (**T4DIM)** which shows an ambipolar semiconducting behavior together with electroluminescence in single-layer OLET device architecture[14]. This organic semiconductor is characterized by end substitution of a bithiophene core with two strong electron-withdrawing thieno(bis)imide moieties. Despite the numerous structures realized so far (i.e. of different sizes, substitutions, shapes, etc..)[11] materials combining both ambipolar charge transport and efficient electroluminescence are still a synthetic challenge, as these properties typically exclude one another in the solid state[12]. In this context, the substitution of oligothiophene materials[13-14] with strong electron-withdrawing moieties as for instance thieno(bis)imide units resulted as a powerful tool to obtain also electron transporting polythiophenes.

In this thesis I cross-correlate photoluminescence spectroscopy and morphological investigation in order to gain fundamental information on the T4DIM thin-film supra-molecular organization, given that photoluminescence spectroscopy has proven to be a powerful and highly sensitive technique to probe how the electronic structure and energy transport processes in conjugated molecules are modulated by aggregation in solid state. In this way, it is possible to provide feedback to the deposition conditions of the active material (i.e. deposition rate, substrate nature,..) for improving device electrical and light-emission performances.

The thesis is organized as follows:

In *chapter 1* an introduction on organic semiconductors is presented together with a general description of the OLET device. Optical and electrical properties are described in more details by introducing the theory of excitons in organics introducing excitonic processes single crystals and thin films as case study.

In chapter 2 the experimental setups used for performing low temperature steady-state and time-resolved photoluminescence (PL) spectroscopy and PL quantum yield

measurements. Moreover, a detailed description of the atomic force microscopy (AFM) and confocal laser scanning microscopy (CLSM) which are implemented in the morphological investigations of thin-films is reported

In *chapter 3*, the synthetic route of T4DIM is reported, together with its photo-physical properties in solution of T4DIM. In particular, a detailed study of the effects of different organic solvents on the emission properties of T4DIM is carried out by means of steady-state and time resolved PL spectroscopy. In order to support and rationalized our experimental data, complementary density-functional theory (DFT) based calculations are performed.

In *chapter 4*, the photo-physical properties of T4DIM thin-films grown at different conditions are investigated. The study is held by cross-correlating a detailed time-resolved and energy-dispersed PL spectroscopy (2 ps time resolution) at low temperature with morphological probing tools such as AFM and CLSM. The results are presented in two distinct sections as follows:

In the first section, I studied the dependence of the molecular arrangement T4DIM in thin films when sublimated onto different technologically-relevant substrates.

In the second section, T4DIM was vacuum-sublimed onto PMMA/ITO/glass substrate at different layer thickness (from monolayer to multilayer) and at different evaporation rates in order to modulate in thin-films the interplay between the molecular self-organization and kinetics of growth.

References

[1] Forrest, S. R. The Path to Ubiquitous and Low-Cost Organic Electronic Appliances on *Plastic. Nature* **2004**, 428, *911–918.*

[2] Meijer, E. W.; Schenning, A. P. H. J. Chemistry: Material Marriage in Electronics. *Nature* **2002**, 419, *353–354.*

[3] Mishra, A. & Bauerle, P. *Angew. Chem. Int. Ed.* (**2012**), 51, 2020-2067

[4] Roncalli, J. *Acc. Chem. Res.* (**2009**) 42, 1719-1730

[5] Cheng, Y.J. Yang, S.H. & Hsu, C. S. *Chem. Rev.* (**2009**), 109, 5868-5923

[6] Beaujuge, P.M. & Fréchet J. M. J.*J.Am. Chem. Soc.*(**2011**), 133, 20009-20029

[7] Zachary B. Henson, Klaus Mullen and Guillermo C. Bazan *Nature Chemistry* (**2012**), 4, 699-704

[11] (a) Arias, A. C.; MacKenzie, J. D.; McCulloch, I.; Rivnay, J.; Salleo, A. *Chem. Rev.* **2010**, *110*, 3; (b) Tsao, H. N.; Mu□llen, K. *Chem. Soc. Rev.* **2010**, *39*, 2372; (c) Usta, H.; Facchetti, A.; Marks, T. J. *Acc. Chem. Res.* **2011**, *44*, 501; (d) Wang, C.; Dong, H.; Hu, W.; Liu, Y.; Zhu, D. *Chem. Rev.* **2012**, *112*, 2208; (e) Mishra, A.; Ma, C.-Q.; Baüerle, P. *Chem. Rev.* **2009**, *109*, 1141; (f) Barbarella, G.; Melucci, M.; Sotgiu, G. *Adv. Mater.* **2005**, *17*, 1581;

[12] (a) Perepichka, I. F.; Perepichka, D. F.; Meng, H.; Wudl, F. *Adv. Mater.* **2005**, *17*, 2281; (b) Taranekar, P.; Qiao, Q.; Jiang, H.; Schanze, K. S.; Reynolds, J. R. *J. Am. Chem. Soc.* **2007**, *129*, 8958; (c) Smith, M. B.; Michl, J. *Chem. Rev.* (**2010**), *110*, 6891; (d) Najafov, H.; Lee, B.; Zhou, Q.; Feldman, L. C.; Podzorov, V. *Nat. Mater.* (**2010**), *9*, 938.

[13] (a) A. Mishra, C.-Q. Ma and P. Ba¨ uerle, *Chem. Rev.*, (**2009**), 109, 1141; (b) G. Barbarella, M. Melucci and G. Sotgiu, *Adv. Mater.*, (**2005**), 17, 1581.

[14] Manuela Melucci et al. *Chem. Commun.*, (**2011**), **47**, 11840–11842.

Chapter 1

Organics Semiconductors

This chapter provides a brief description of the structure, the electrical and optical properties of organic semiconductors. In the introduction the chemical structure of these materials and the intermolecular forces in the solid state are presented. To establish the context of this thesis, emphasis is given to the concept of exciton and its role in determining the optical properties.

Introduction

The name *organic semiconductor* denotes a class of materials based on carbon, that display semiconducting properties. The common characteristic of these materials resides in the molecular electronic structure that is based on π-conjugated double bonds between carbon atoms. The delocalization of the electrons in the π molecular orbitals is the key feature, that allows injection, delocalization and transport of charges. The π-conjugated materials can be divided into two main classes according to their molecular weight (MW). Low MW organic semiconductors are usually named *small molecules*, whereas π-conjugated polymers have MW reaching many thousands of *g/mol*. The possibility of using small molecules and polymeric organic materials for applications in the electronics and semiconductor industry has been of great scientific and technological interest for several decades[15]. While for many years electronics materials research has been dominated by the impressive performance of inorganics, the attraction of organics or plastic electronics is driven by the possibility of enabling new applications by circumventing some of the limitations of inorganics materials, and more importantly, of achieving more comparable device performance but at considerably reduce cost[16].

Figure 1.1 shows the chemical structure of some of the low MW most studied organic semiconductors. They can be classified as linear, two-dimensional fused ring compounds, and heterocyclic oligomers. However, while the design, synthesis, and structure–property relationships of *p*-type organic semiconductors have been widely investigated *n*-type oligomeric and are still not fully developed.
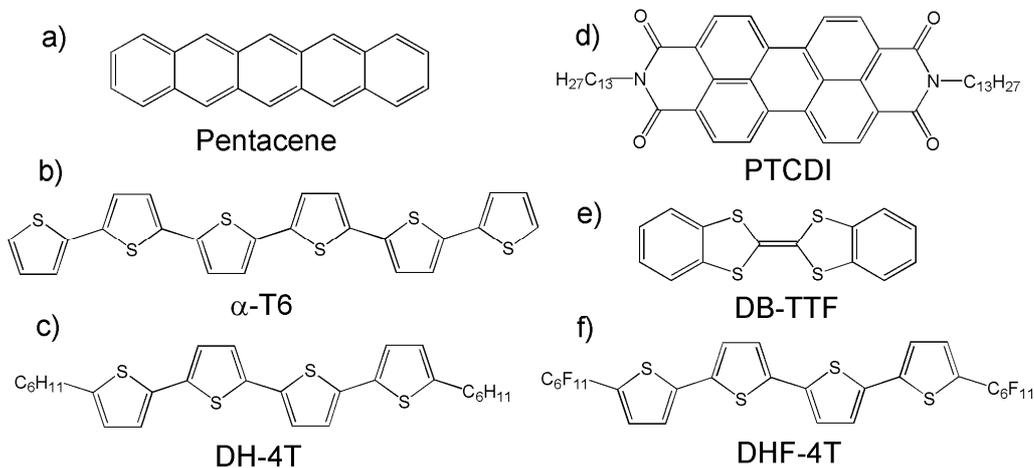
Figure 1.1 *Small molecule semiconductors, which are commonly known for their hole and electron channel characteristics in field-effect transistors. a) Pentacene, b) hexathiophene, c) α,ω-dihexyl-quaterthiophene, d)N,N'-ditridecyl-3,4,9,10 perylenetetracarboxylicdiimide, e)dibenzotetrathiafulvalene, f) α,ω-diperfluorohexyl-4T*

A number of design rules have guided the search so-called for the *n-type* semiconductors. In order to be able to inject electrons into the LUMO level from environmentally stable electrodes, such as gold, the LUMO level must be lowered (i.e., increasing the electron affinity) substantially in order to align with the work function of the metal. At the same time, increasing the electron affinity of a semiconducting material also improves its environmental stability, that is, its sensitivity to oxygen and water. On the basis of known *n*-channel transistors, it was generally assumed that a high electron affinity (at least 3 *eV*) is necessary to observe *n*-channel behavior[17]. This is achieved by taking a known semiconducting core molecule and adding strong electron withdrawing groups such as fluorine, cyano, or diimide moieties. In addition to stability and energetic considerations, the orientation of molecules to each other and the associated transfer integrals of electrons play a role. The best LUMO-LUMO overlap for electron transport may be different from the ideal HOMO-HOMO overlap for hole transport[18,19]. Facchetti et al. showed that the molecular packing in crystalline semiconductors can strongly affect the observation of *p*- or *n*-channel characteristics[20,21].

1.2 Optical Properties in solid state

Many, but not all, spectral properties of small aggregates and crystals are directly traceable to properties of individual molecules. However the energy of interaction between the molecules weak as it be, impose a communal response upon the molecular behavior in the aggregates, the collective response is embodied in an entity called exciton. Excitons represent bound electron–hole pairs, that may be generated by absorption of light or by relaxation of free electrons and holes after optical or electrical pumping. Among the optical properties of exciton systems that have aroused much interest, are cooperative spontaneous emission[22,23] (*including application in light-emitting diodes*[24] *and lasers*[25]), strong optical nonlinearities[26–28], and optical bistability[29]. Excitons are usually distinguished in two classes: *Frenkel* excitons and *Wannier–Mott* excitons[30] (*Figure 1.2*). The distinction lies in the typical separation between electron and hole. For Frenkel excitons, this separation is essentially zero (*electron and hole occur on the same molecule or atom*) and their binding energy is large *(~1 eV)*. For the Wannier–Mott exciton the electron–hole separation is much larger than a single molecule or atom and the binding energy is small *(~1 meV)*. Physically, the distinction originates from the competition between two energy scales: the electron–hole coupling and the rates for electron and hole hopping between different molecules or atoms[31].

Frenkel   Wannier   Charge-transfer
exciton   exciton   exciton
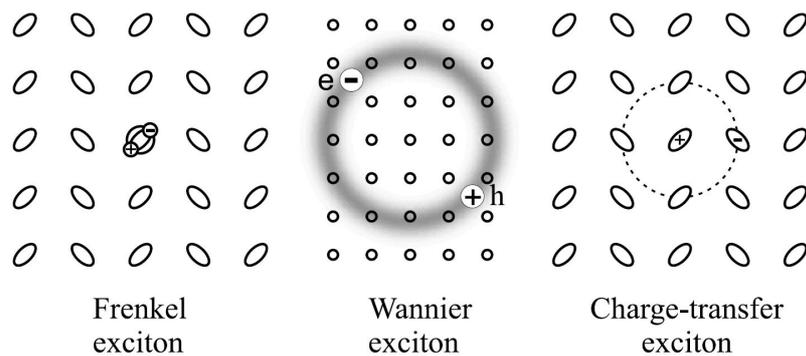
Figure 1.2 *Classification of excitons on the basis of the electron-hole pair radius.*

While the names Frenkel and Wannier–Mott excitons refer to two extreme cases with regards to the length scale of relative electron–hole motion (the internal exciton structure), this scale in practice does allow for all the intermediate cases. The intermediate case that has acquired a special status is the charge-transfer exciton

CTE, which in its lowest-energy variation has an electron–hole separation of one molecule. Thus, the hole is located at one molecule and the electron on the neighboring one. This is often referred to as a "donor–acceptor (D-A) complex". CTEs may occur in systems with an alternating structure of two types of molecules [16], but also in crystals with just one type of molecule (*such as anthracene, naphthalene, and many others*). In the latter case, any molecule in the crystal can play the role of donor or acceptor. CTEs currently are considered important intermediate states in the photo-conductivity of organic crystals[32]. In this process, they are essential in the creation of free carriers from photo-generated Frenkel excitons.

1.2.1 Excitons in molecular crystals

To account for the dependence of spectroscopic properties on the molecular organization imposed by the solid state, molecular exciton theory has been developed.[33–35] The theory takes into account coupling between transition charge densities associated with transitions between the ground state and singlet excited states localized on individual molecules within the crystal. This coupling results in the formation of delocalized excited states and collective spectroscopic transitions. In crystals containing only one molecule in the unit cell, a positive interaction energy between the transition charge densities of the individual molecules results in a collective spectroscopic transition that occurs at a photon energy higher than the corresponding transition of the isolated molecules. Molecular assemblies showing such a hypsochromically shifted absorption band are commonly referred to as H-aggregates[36]. Conversely if the interaction energy is negative, a collective transition is predicted at photon energies lower than that for the corresponding isolated molecules. Molecular assemblies with such red-shifted absorption bands are classified as J-aggregates. Transition to the upper state is allowed in molecules with cofacial arrangement (H-aggregates) and transition to the lower state is allowed in molecules arranged in head to tail fashion (J-aggregates) *Figure 1.3*
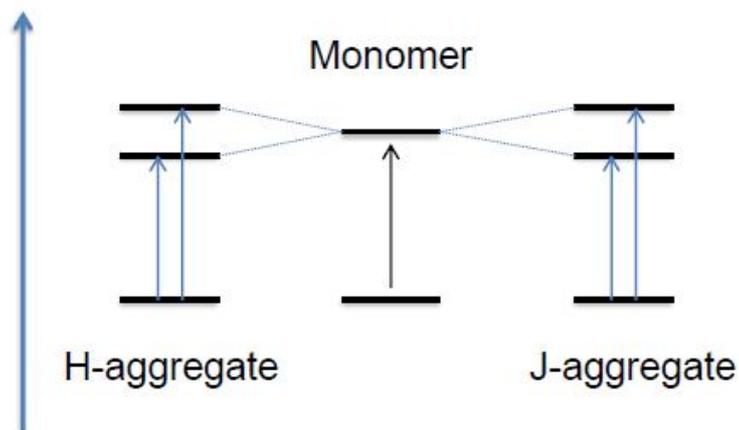
Figure 1.3 *Schematic representation of exciton splitting W of the optically allowed transitions and the splitting energy between excited states both in H- and J-aggregates.*

J-aggregates are the only molecular systems where electronic excitation is delocalized over several molecular units as a result of significant retention of π-overlap between neighboring molecules, giving rise to many cooperative and coherent phenomena, such as giant oscillator strength and superradiance, making such systems strongly emissive[37]. π-Conjugated materials with such orientations can form ideal candidates for optoelectronic devices because they combine both high luminescence and charge-conducting properties of organic molecules.

For crystal structures with n molecules in the unit cell, the maximum number of allowed collective transitions equals n. For crystal structures with two molecules in the unit cell, which is common for aromatic molecules, two optically allowed electronic transitions are expected. Such molecular assemblies can in principle show both *J*- and *H*-type bands. The difference in photon energy between the two allowed transitions is referred to as the *Davydov* splitting (DS). The DS may be regarded as an experimental observable. In doing so, it is important to note that the splitting is not completely determined by the electronic motion. It can also be influenced by motion of the atomic nuclei, especially in the case where the coupling between electronic and vibrational degrees of freedom is strong in comparison to the strength of the excited-state intermolecular electronic coupling. Depending on the particular material and vibronic band under study, the magnitude of the DS can be strongly reduced by the included Franck−Condon factors, accounting for the overlap between vibrational wave functions at ground and excited states. The DS is also influenced by charge transfer interactions between (neighboring) molecules[38].

1.3.1 Exciton generation, diffusion and relaxation

In the previous sections we have shown how the isolated molecule energy levels split to form the exciton band and the Davydov components in a molecular solid. Here we describe how an exciton can be created and discuss the processes it may undergo upon diffusion and relaxation.

Exciton generation

An exciton can be generated exciting the crystal or the thin film with an electromagnetic wave. This light must have a frequency resonant with the energy gap and the right polarization with respect to the transition dipole moments. Moreover, in order to have light absorption and exciton creation optical selection rules must be satisfied. In particular, the photon momentum **q** must be equal to the **k** wave vector. Since in the UV/VIS region q ~ 0, only k = 0 states are probed. If the crystal has an inversion center then states are classified as *gerade* (g) and *ungerade* (u) and only u ← g transition are allowed. Two photon absorption (i.e. absorption of light through a mid gap virtual state), being a second order process, is capable to perform g ← g transitions[39]. An electrical way to generate excitons is by charge carrier recombination. This process involves: the injection of holes and electrons in the material by means of electrodes, their diffusion in the presence of an electric field, charge recombination and exciton formation. In this case both triplet and singlet exciton are created with a ratio 3/1, respectively. Light emission of electrically generated exciton is called electroluminescence and in organic semiconductors was first observed by Pope[40]. Electroluminescence is at the basis of the operation of optoelectronic devices such as OLED[41] and OLET[42].

Exciton diffusion

As pointed out in the definition of exciton, this quasiparticle is characterized by a wave-like motion. This aspect is relevant not only from the fundamental viewpoint of the energy transport but also because of its importance for optimal design of organic thin film electronic device. Immediately after exciton creation, the phases of the wfs of all excited molecules have a unique relationship. If the phases are maintained during the excitation motion, the exciton moves as a wave and is said to be coherent. However, because of the interactions with lattice modes (phonons) and imperfections

(physical and chemical) in the crystal the coherence may be lost. Then the exciton moves with a random hoppinglike behavior. Typical values of the exciton diffusion coefficients for single crystals are $10^{-3} \div 10^{-5}$ cm^2 sec^{-1}. During the hopping movement, excitons can experience sites with an energy below the exciton band. In this case, if the thermal energy is not sufficient to promote the hopping, the exciton is trapped. Then it can relax with emission of radiation or with a non radiative pathway. We neglect here the treatment on high exciton density phenomena such as exciton-exciton annihilation or exciton-polaron interactions since they are not relevant for the experimental results reported in this thesis. A detailed review of these processes in organic semiconductor can be found in reference [i1].

Exciton relaxation

There are many pathways that an exciton can undergo in order to relax to the fundamental ground state. The investigation of the energetics and the dynamics involved in these processes is the fundamental question of solid state photophysics. Since this thesis focuses on the photophysical properties of T4DIM in the solid state, we will discuss in detail all the processes relevant for this material, though with a general approach. *Figure 1.4* show an energy diagram of the different relaxation pathway for an exciton.
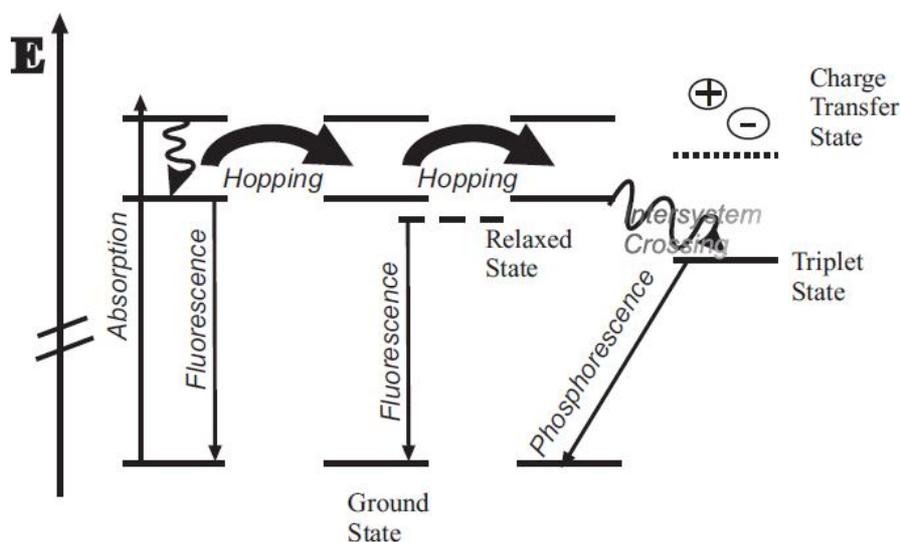
Figure1.4 Energy diagram for a molecular solid with two Davydov components, a charge transfer state and a relaxed state. Upward arrow show the absorption of light with an energy matching the higher Davydov band. Thick bend arrows show the exciton hopping between adjacent molecular sites. Curved downward arrows show nonradiative processes while straight downward arrows represent radiative processes.

Initially, light with a resonant frequency is absorbed and an exciton is created in the upper or lower Davydov component (upward arrow) according to frequency and polarization. Few hundred of femtoseconds later the exciton can either relax to the lowest Davydov component (curved arrow) or it can hop to the nearest sites (thick bend arrow) and eventually dissociate to form a charge transfer state. All these early stage processes are non radiative and are usually probed with ultrafast pump and probe spectroscopies[43]. It is important to point out here that, due to the Kasha rule, radiative relaxation always takes place from the lowest state of the exciton band. As a consequence, we expect light emission from the lowest excitonic level and eventually from "relaxed states" that lie just below the exciton band. In *Figure 1.4* it is shown that is possible to observe fluorescence (downward arrow) from the above mentioned states and eventually phosphorescence (oblique arrow) from triplet exciton states. All the transitions illustrated in *Figure x* are characterized by a rate constant k that is the sum of at least two components $k = kr + knr$. In the case of fluorescence the measured lifetime is the reciprocal of k. In order to obtain kr equation can be used provided that the fluorescence quantum yield (Φ_F) is known. $kr = \Phi_F k$ In this thesis we will use the term photoluminescence (PL) as a synonymous of fluorescence.

1.3 Electrical Properties.

For an organic semiconductor the key quantity that characterizes charge transport is the carrier mobility. Although these do not directly concern with the experiments and with the results reported in this thesis, it is important to have an overview of all the physical/chemical properties of organic semiconductors. In the absence of any external potential, transport is purely diffusive and is generally described by a simple diffusion equation:

$$\langle x^2 \rangle = nDt$$

where $\langle x^2 \rangle$ denotes the mean-square displacement of the charges, D is the diffusion coefficient, t is the time, and n represents an integer number equal to 2, 4, or 6 for one-, two-, and three-dimensional (1D, 2D, and 3D) systems, respectively.

As one applies an electric field to a semiconductor, the electrostatic force causes the carriers to first accelerate and then reach a constant average velocity, v, due to collisions with impurities and lattice vibrations. The ratio of the velocity to the

applied field is called the mobility. Diffusion should be seen as a local displacement of the charge around an average position, while drift induces a displacement of the average position. Drift is the effect that dominates the migration of the charges across an organic layer in the devices. The carrier mobility is usually expressed in $cm^2/V \cdot s$ (since it corresponds to velocity over electric filed) *Figure 1.5.*
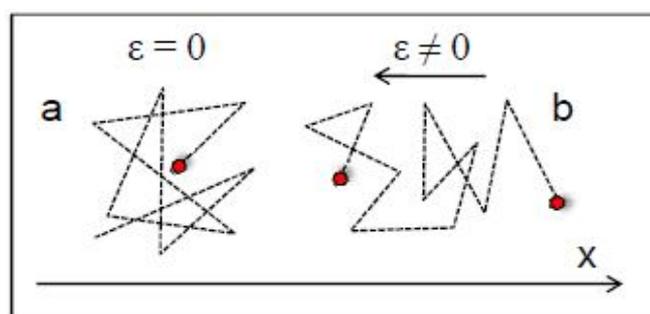
Figure 1.5 *The carrier motion in the semiconductor in the absence and in the presence of an electric field.*

It is natural to imagine the process of charge transport in a organic semiconductor as a series of redox events, where the charge residing on one molecule is transferred to the next one as in the scheme below, valid for one dimensional chain of identical molecules where an electron has been removed:

…AA+AA… → …AAA+A…
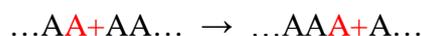
The charge mobility so can be described by sequential hopping between molecules and the maximum value can be express in terms of physical quantities that are all experimentally accessible. The evaluation of the maximum hopping mobility with realistic parameters suggest that sequential charge hopping is not the correct transport mechanism for the best molecular material used in organic transistor[44]. The simple hopping transport model, made very common in the chemistry by its simplicity and by analogy with redox chemistry, is in practice never valid for the hights crystalline material. The exact nature of charge transport in organic semiconductors is still open to debate. Nevertheless, one can make a clear distinction between disordered semiconductors such as amorphous polymers and highly ordered organic single crystals, at the opposite ends of the spectrum. Charge transport in disordered semiconductors is generally described by thermally activated hopping of charges through a distribution of localized states or shallow traps. For highly ordered molecular crystals such as, e.g., rubrene, tetracene, and pentacene, however,

experimental data seems to exclude hopping transport. Temperature-dependent time-of-flight[67] and time-resolved terahertz pulse spectroscopy[46,47], measurements on high purity crystals showing high mobilities that increase with decreasing temperature, suggest bandlike transport in delocalized states instead of hopping transport. Models for charge transport in organic semiconductors, such as polycrystalline thin films of small molecules and microcrystalline polymers that lie in between these two extreme cases, have been proposed as well[48-50]. Note that in all cases the transfer integral representing the electronic coupling of adjacent molecules and the polaronic relaxation energy, which is the energy gained when a charge geometrically relaxes over a single molecule or polymer segment, is an important parameter determining the probability of charge transport from one molecule to another and depends strongly on the particular molecule and the relative position of the interacting units.

1.4 Overview on OLETs devices

Organic Light-Emitting Field-Effect transistors (OLETs) are emerging as an innovative class of multifunctional devices that integrates the electronic properties of a transistor, the light generation capability and the full potential of organic photonics. The most advanced OLET structures encompass a huge technological potential for the realization of intense nanoscale light sources and highly integrated optoelectronic multifunctional systems. As for a traditional field-effect transistor (*organic or inorganic*) an OLET device requires the following components (shown in *Figure 1.6*): a thin semiconducting layer, which is separated from a gate electrode by the insulating gate dielectric; source and drain electrodes of width *W* (channel width) separated by a distance *L* (channel length) that are in contact with the semiconducting layer.
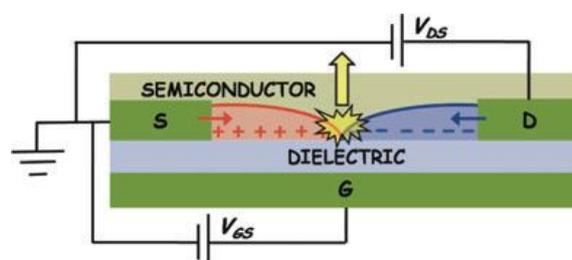
Figure 1.6 *Schematic of an organic light-emitting field-effect transistor with the constituent components.*

In an ambipolar transistor both holes and electrons are simultaneously injected in the channel by the source and drain electrodes at a suitable gate bias that has to be higher in absolute value with respect to the hole and electron gate threshold voltages. In the case of ideal ambipolar transistor with only one semiconducting layer, the ambipolar regime is characterized by a hole and an electron accumulation layer that meet at some point within the transistor channel. The position of the electroluminescence emission region is moved within the channel according to the applied gate and source-drain voltages and the charge-carrier mobility ratio. So, the micrometer separation between the emission area and the injecting electrodes in ambipolar OLETs leads to improved emission quantum efficiency due to the decreased photon losses.Most of the single-layer organic field-effect transistors that have been fabricated to date show only unipolar conduction (either holes or electrons) even though in principle pure organic semiconductor should support both electron and hole transport equally[51].Given the limited number of electroluminescent materials with good ambipolar mobility values, different device architectures are to be implemented to achieve high ambipolar transport in OLETs

1.4.1 Working Principle of OFETs

Since throughout this thesis we deal only with bottom gate-top contact configuration (*Figure x*), we use this simple configuration to discuss briefly how a classic OFET works. We refer to the voltage applied between drain and source as *Vds*, while the voltage applied to the gate is labeled as V_{gs}. By convention, the source is generally considered grounded and the voltage is applied to the drain contact. The current flowing through the channel is called I_{ds} and it is a strong function of V_{gs}. The dielectric is sandwiched between the gate and the organic semiconductor, and they work as two plates of a plane capacitor. Thus, when a V_{gs} is applied, charges of different sign are accumulated at gate/dielectric and dielectric/organic semiconductor interfaces. Much of this accumulated charge in the active material is mobile and moves in response to the applied V_{ds}. When no V_{gs} is applied there are ideally no free charge carriers, and the device is off. Otherwise, with applied V_{gs} the device is on. This gate-induced charge carrier creation is called field-effect, and it is the key-idea

of the working principle of FETs[52]. An n-channel OFET (i.e., electrons are transported through the channel) can be used as an example to understand the basic device operational regimes due to the gate voltage dependence of the distribution of "free" charges in the active material[53]. If we assume ohmic contacts and no trap presence (ideal case), when a $V_{gs} > 0$ is applied, free electrons start accumulating at organic semiconductor/dielectric interface. Without any voltage difference between drain and source ($V_{ds} = 0$), this negative charge density is uniform along all the active material, thus having a uniform conduction channel. If a positive V_{ds} is applied, the induced charge superficial density in a certain position x of the semiconductor is described by Eq. (1):

$$qind = n(x)et = Ci\,[Vgs - V(x)] \text{ (Eq.1)}$$

where t is the thickness of the charge layer in the channel, $n(x)$ is the number density of charges in the channel, e is the electron charge and C_i is the insulator capacitance per area unit. However, real devices are far from being ideal and not all induced charges are mobile; a large number of deep charge traps are present in the film (deep enough to effectively immobilize electrons trapped in them). Deep traps have to be filled before the additionally induced charge can move. Thus, a minimum gate voltage has to be applied to obtain free electron density in the channel, the threshold voltage, Vth. If we include the threshold voltage in the previous equation:

$$qind = n(x)et = C_i\,[V_g - V_{th} - V(x)] \text{ (Eq.2)}$$

As V_{th} is not ideally a function of x, with $V_{ds} = 0$ and $V_{gs} > V_{th}$ a homogeneous charge density is present in the channel. When a small source-drain voltage is applied ($V_{ds} << V_{gs} - V_{th}$) a linear gradient of charge density is formed. The voltage drop between organic semiconductor and gate is larger at the source, where $V(x) = 0$ (grounded), than at the drain, where $V(x) = Vds$. This is the linear regime in which the current flowing through the channel is directly proportional to V_{ds} (*Figure1.7a*). When the source-drain voltage is further increased, we reach a point where a potential difference between the gate and the part of the channel near the drain no longer exists, the channel is pinched off. This means that a charge carrier depletion region is formed next to the drain, because the difference between the local potential $V(x)$ and V_{gs} is lower than the threshold voltage. A space-charged-limited saturation current can flow across this narrow depletion zone. Carriers are swept from the pinch point to the drain by a comparatively high electric field in the depletion region (*Figure 1.7b*). A further increase in V_{ds} pushes the pinch-off point further away from

the drain (*Figure 1.7c*). However the length of the channel (L) shortens only slightly, as it is infinitely larger than the width of the depletion region, and the integrated resistance of the channel from the source to the pinch point remains more or less the same.
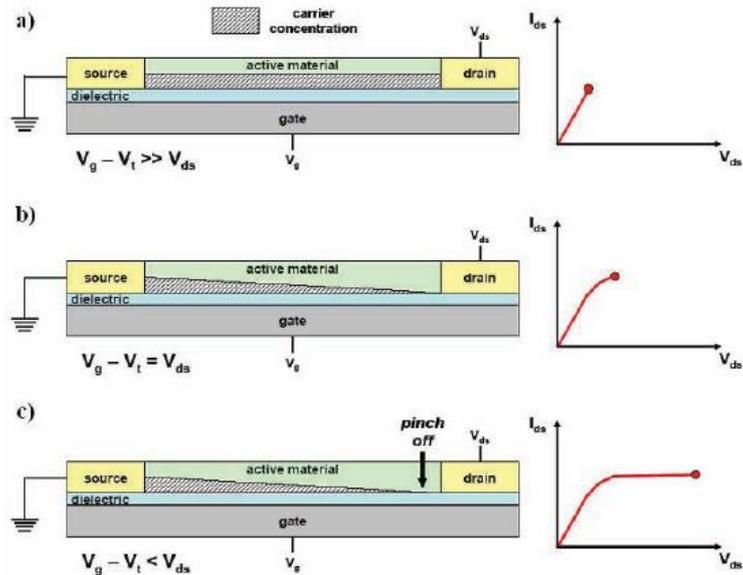
Figure 1.7. *Schematic structure of an OFET. a) Carrier concentration profile in the linear regime; b) Carrier concentration profile when the pinch off occurs near the drain electrode (Vgs–Vth=Vds); c) Carrier concentration profile in the saturation regime.*

For these reasons once pinch off condition is met, current saturates at I^{sat}_{ds} . From a mathematical point of view, pinch off is reached when $V_{ds} = V_{gs} - V_{th}$. The current-voltage characteristics in the different operating regimes of an OFET can be described analytically, in a simplistic way assuming that (1) the transverse electric field induced by the gate voltage is largely higher than the longitudinal field induced by the gate bias (gradual channel approximation) and (2) the mobility is constant all over the channel. In short, current-voltage characteristics can be drawn by either varying the drain voltage at a constant gate voltage (output characteristics) or changing the gate voltage at a fixed drain voltage (transfer characteristics). Locus characteristics are obtained by varying simultaneously drain voltage and gate voltage and keeping them at the same value so that the pinch-off condition is always reached in the reached the drain electrode. In the output characteristics, the curves are divided into a linear regime at low V_{ds} that turns into the saturation regime when $V_{ds} > V_{gs}$. The current I_{ds} in both regimes is given by the equations (x) and (x) :

$$I_{ds}^{lin} = \frac{W}{L} C_i \mu \left[(V_{gs} - V_{th})V_{ds} - \frac{V_{ds}^2}{2} \right] (Eq.\,3) \; Linear \; regime$$

$$I_{ds}^{sat} = \frac{W}{2L} \, C_i \mu \left(V_{gs} - V_{th} \right)^2 \quad (Eq.4) \; Saturation \; regime$$

in which μ is the charge carrier mobility.

References

[15] (a) *Organic Electronic Material: Conjugated Polymers and Low Molecular Weight Organic Solids* (Eds: R. Farchioni, G. Grosso) *Springer, Berlin* **2011.** (b) S.R. Forrest, *Nature* **2004**, 428,911 (c) T.W.Kelly, et al. *Chem. Mater.* 2004, 16, 4413.

[16] Printed Organic And Molecular Electronics (Eds: D.Gamota, P.Brazis, K.Kalyanasundaram, J.Zhang), Kluwer Academic, Boston, MA **2004**.

[17] Bernius, M. T.; Inbasekaran, M.; O'Brien, J.; Wu, W. S. *Ad*V. *Mater.* (**2000**), *12*, 1737.

[18] Becker, H.; Spreitzer, H.; Kreuder, W.; Kluge, E.; Schenk, H.; Parker, I.; Cao, Y. *Ad*V. *Mater.* (**2000**), *12*, 42.

[19] Jurchescu, O. D.; Baas, J.; Palstra, T. T. M. *Appl. Phys. Lett.* (**2004**), *84*, 3061.

[20] Chua, L. L.; Zaumseil, J.; Chang, J. F.; Ou, E. C. W.; Ho, P. K. H.; Sirringhaus, H. R.; Friend, H. *Nature* (**2005**), *434*, 194.

[21] Dimitrakopoulos, C. D.; Malenfant, P. R. L. *Ad*V. *Mater.*(**2002**), *14*, 99.

[22] M. Kasha, in: B. di Bartolo (Ed.), *Spectroscopy of the Excited State*, Vol. B12, Plenum, NewYork, (**1976**).

[23] S. de Boer, K. Vink, D.A. Wiersma, *Chem. Phys. Lett.* 137 (**1987**) 99.

[24] N.C. Greenham, S.C. Moratti, D.D.C. Bradley, R.H. Friend, A.B. Holmes, *Nature* 365 (**1993**) 628.

[25] U. Lemmer, A. Haugeneder, C. Kallinger, J. Feldmann, in: G. Hadziioannou, P.F. van Hutten (Eds.), Semiconducting Polymers, Wiley-VCH, Weinheim, (**2000)**.

[26] B.I. Greene, J. Orenstein, S. Schmitt-Rink, *Science* 247 (**1990**) 679.

[27] V.L. Bogdanov, E.N. Viktorova, S.V. Kulya, A.S. Spiro, *Pis'ma Zh. Èksper. Teoret. Fiz.* 53 (1990) 100; *JETP Lett.* 53 (**1991**) 105.

[28] Y. Wang, *J. Opt. Soc. Amer. B* 8 (**1991**) 981.

[29] H.M. Gibbs, Optical Bistability: Controling Light with Light, Academic Press, New York, (**1985)**.

[30] R.S. Knox, *Theory of Excitons*, Academic Press, New York, (**1963)**.

[31] H. Haken, *Quantum Field Theory of Solids*: An Introduction, North-Holland, Amsterdam, **1976**.

[32] M. Pope, C.E. Swenberg, Electronic Processes in Organic Crystals and Polymers, Oxford University Press, Oxford, (**1999**).

[33] Davidov, A. S. *Theory of Molecular Excitons*; Plenum Press: New York, (**1971**).

[34] Philpott, M. R. *Some Modern Aspects of Exciton Theory*. In Advances in Chemistry and Physics; Prigogine, I., Rice, S. A., Eds.; J.Wiley: Hoboken, NJ, (**1973**); Vol. 23.

[35] Agranovich, V. M. *Excitations in Organic Solids*; Oxford University Press: Oxford, U.K., (**2009**).

[36] Spano, F. C. *Acc. Chem. Res.* (**2010**), 43, 429−439.

[37] Da Como, E.; Loi, M. A.; Murgia, M.; Zamboni, R.; Muccini, M. J-Aggregation in R-Sexithiophene Submonolayer Films on Silicon Dioxide. *J. Am. Chem. Soc.* **2006**, 128, 4277–4281

[38] Yamagata, H.; Norton, J.; Hontz, E.; Oliver, Y.; Beljonne, D.; Brédas, J. L.; Silbey, R. J.; Spano, F. C. *J. Chem. Phys.* (**2011**), 134, 204703 1−11.

[39] N. Periasamy, D. Danieli, G. Ruani, R. Zamboni, and C. Taliani, "Location of the low-energy Ag1 state in a polythiophene oligomer by 2- photon absorption-spectroscopy: alpha-sexithienyl," *Phys. Rev. Lett.*, vol. 68, pp. 919–922, **1992**.

[40] M. Pope, H. Kallmann, and P. Magnante, "Electroluminescence in organic crystals," *J. Chem. Phys.*, vol. 38, pp. 2042–2043, **1963**.

[41] S. R. Forrest, "Ultrathin organic films grown by organic molecular beam deposition and related techniques," *Chem. Rev.*, vol. 97, pp. 1793–1896, **1997**.

[42] C. Rost, S. Karg, W. Riess, M. A. Loi, M. Murgia, and M. Muccini, "Ambipolar light-emitting organic field-effect transistor," *Appl. Phys. Lett.*, vol. 85, pp. 1613–1615, **2004**.

[43] G. Lanzani, S. V. Frolov, P. A. Lane, Z. V. Vardeny, M. Nisoli, and S. De Silvestri, "Transient spectroscopy of Frenkel and charge transfer excitons in alpha-sexithienyl films," *Phys. Rev. Lett.*, vol. 79, pp. 3066 – 3069, (**1997**).

[44] A. Troisi, *Organic Electronics* **2011**, 12, 1988-1991

[45] Warta, W.; Stehle, R.; Karl, N. *Appl. Phys. A: Mater. Sci. Process.* (**1985**), *36*, 163.

[46] Ostroverkhova, O.; Cooke, D. G.; Shcherbyna, S.; Egerton, R. F.; Hegmann, F. A.; Tykwinski, R. R.; Anthony, J. E. *Phys. ReV. B* (**2005**), *71*, 035204.

[47] Ostroverkhova, O.; Cooke, D. G.; Hegmann, F. A.; Anthony, J. E.; Podzorov, V.; Gershenson, M. E.; Jurchescu, O. D.; Palstra, T. T. M. *Appl. Phys. Lett.*(**2006**), *88*, 162101.

[48] Horowitz, G. *J. Mater. Res.*(**2004**), *19*, 1946.

[49] Sirringhaus, H. *Ad*V. *Mater.* (**2005**), *17*, 2411.

[50] Salleo, A.; Chen, T. W.; Volkel, A. R.; Wu, Y.; Liu, P.; Ong, B. S.; Street, R. A. *Phys. Re*V. *B* (**2004**), *70*, 115311.

[51] N. Karl, *Synth. Mater.* 133–134, 649 (**2003**).

[52] C. R. Newman, C. D. Frisbie, D. A. da Silva Filho, J. L. Bredas, P. C. Ewbank, and K. R. Mann. Introduction to organic thin film transistors and design of n-channel organic semiconductors. *Chem. Mater.*, 16:4436–4451, (**2004**).

[53] J. Zaumseil and H. Sirringhaus. Electron and ambipolar transport in organic field-effect transistors. *Chem. Rev.*, 107(4):1296, (**2007**).

Chapter 2

Experimental setup

In this chapter a description of the experimental setups used to prepare thin films of T4DIM and to perform steady state photoluminescence at low temperature, time resolved PL spectroscopy and quantum yield measurements are reported. The chapter includes also a brief introduction to optical microscopy and an overview on atomic force microscopy.

2.1 Quantum yield measurement.

The external radiative quantum efficiency, η, is defined by Equation 5.

η = (*number of photons emitted*) / (*number of photons absorbed*)   (*Eq.5*)

PL efficiency measurements in solution are relatively simple because it is usually appropriate to assume an isotropic angular distribution for the emission. However, this is not true for thin solid films. For molecular and polymeric materials, anisotropy in the distribution of chromophores leads to an anisotropy in the emission dipole-moment. In addition, wave-guiding effects also modify the angular distribution of the emission. A summary of the traditional methods for measuring η has been given by Demas[54]. A popular method is the comparison of fluorescence emission spectra from two solutions one of which is a standard. Quantum yield measurement with *Integrating Sphere* of anisotropic films were first discussed by DeMello[55]. An integrating sphere is a hollow sphere which has its inner surface coated with a diffusely reflecting material (typically barium sulfate). When a light source is placed in an ideal integrating sphere, the light is redistributed isotropically over the sphere interior-surface regardless of the angular dependence of the emission[56]. Hence, if N_Ω photons are detected over a solid-angle Ω, the total number of photons emitted, N, is given by Equation 6.

$$\mathbf{N} = \mathbf{N}_\Omega(4\pi/\eta) \qquad (Eq.6)$$

The basic experimental set up is shown in *Figure 2.1*. An optical fiber leads from the wall of the sphere to a grating spectrometer with a CCD. Immediately in front of the optical fiber is a baffle coated with barium sulfate to prevent direct illumination of the optical fiber. Laser illumination of appropriate wavelength is directed into the sphere through a small entrance hole. Three measurements are made using the sphere. For the first measurement, *Figure 2.1a*, the sphere is empty and laser light alone is detected by the spectrometer. For the second measurement, *Figure 2.1b*, the sample is placed inside the sphere and the laser beam is directed on to the sphere wall. The third measurement, *Figure 2.1c*, is similar to the second, except that the collimated laser beam is now directed on to the sample (the sample is oriented such that laser light reflected from the surface of the sample is directed onto the sphere wall and not back through the entrance hole).
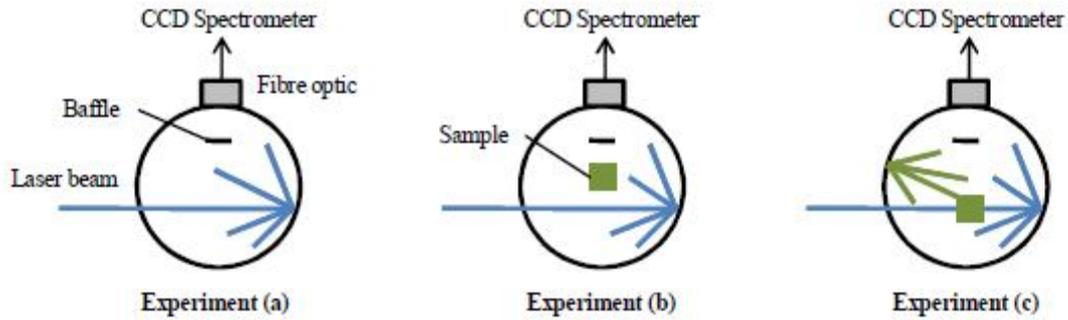
Figure 2.1 Diagram illustrating the three configurations of the sphere required for the efficiency measurement: a) the sphere is empty: b) the sample is in place and the laser beam is directed onto the sphere wall; c) the sample is in place and the laser beam is directed onto the sample.

The total amount of laser light striking the sample can be separated into two contributions. The first is the incident laser beam which strikes the sample directly and locally. The second is diffuse laser light which has scattered from the wall of the sphere and subsequently strikes the sample over its entire surface. After these measurements the value of the quantum yield is given by follow Equation 7 :

$$\eta = \frac{P_c - (1-A)P_b}{L_a A} \qquad A = \frac{L_b}{L_c}$$

where L_a, L_b and L_c are the intensities of the laser beam during the three measurement mentioned above, while Pb and Pc are the intensity related to the photoluminescence of the sample in the experiments *b* and *c* respectively.

2.2 Steady State Photoluminescence at low temperature

Photoluminescence (PL) is the spontaneous emission of light from a material under optical excitation. The excitation energy and intensity are chosen to probe different regions and excitation concentrations in the sample. In organic semiconductor systems, the most common radiative transition is between the HOMO-LUMOstates, with the energy difference being known as the bandgap. The basic elements of a PL spectroscopy set-up consist in an optical source, a sample holder and a photonic multichannel analyzer (PMA). The PMA is a compact spectral measurement apparatus that combines a spectrometer and optical detector into one unit. In our measurement we used as optical source a He-Cd laser that is capable of producing both a UV and visible light at 325 and 442 *nm* respectively and a diode laser at 375*nm* wavelength excitation.
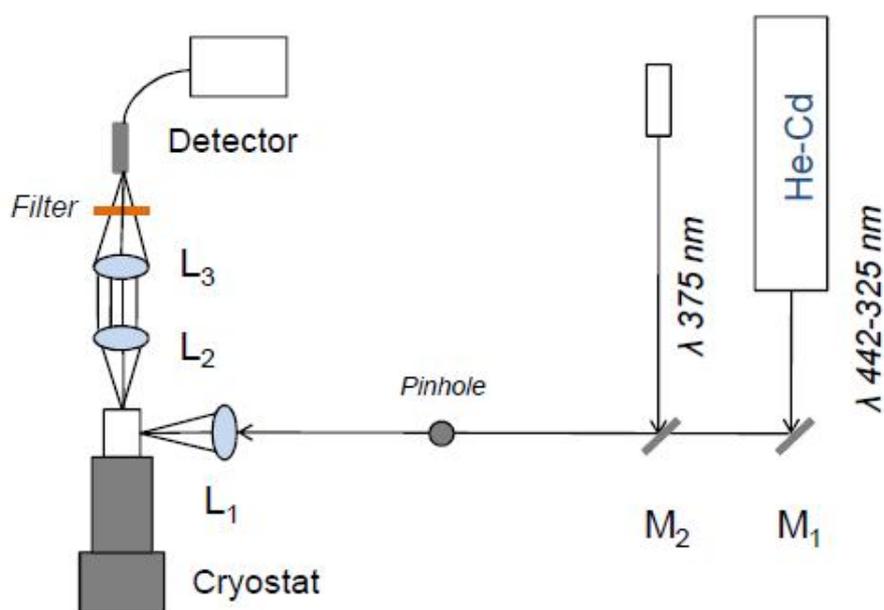
Figure 2.2 *Schematic diagram for PL measurements at low temperature.*

A typical PL set-up is shown in *Figure 2.2* The easiest way to describe the optics of the experiment is to follow the light beam. As it leaves the laser, a mirror are used for alignment the beam through a pinhole that improves the uniformity and the power of the beam. Then the excitation laser beam is focused on the sample with a lens L_1 of typically *f*=20-30 *cm* focal length. The emitted light can be collected by two plano-convex achromatic lenses L_2 and L_3. An achromatic lens, also referred to as an

achromat, typically consists of two optical components cemented together, usually a positive low-index (crown) element and a negative high-index (flint) element. This design permits an improvement in performance because the chromatic aberration of one is counterbalanced by that of the other. The combination of the two lenses L_2 and L_3 each working at infinite conjugation ratio, but with the convex surface toward the focus, has the advantage to reduce the spherical aberration. Moreover in order to improve the collection efficiency of the emitted light a short focal length for L_2 lens is used. While, L_3 can be chosen in order to match the optical aperture of the detector, avoiding unnecessary supplementary losses. For PL measurement at low temperature the sample holder is a vacuum cryogenic pump with high refrigerating capacity in the range of 6 to 320 *K*. A schematic description of that system is given in *Figure 2.3*. From left to right it consists of: a compressor at room temperature and three heat exchangers X_1 (which dumps heat to room temperature T_H), X_L at the low temperature T_L (which absorbs the useful cooling power Q_L) and X_3 (rejecting heat to room temperature). Then a regenerator (which contains a porous matrix that absorbs heat from the gas when it flows to the right, and gives off the heat again when it flows to the left), a tube (which is basically noting more than a tube in which the gas moves back and forth), and orifice O_1 (in principle this is a pure flow resistance adjusted to give the optimum performance). The working medium usually is helium. An extensive explanation of the operation of PTRs is given in[57].
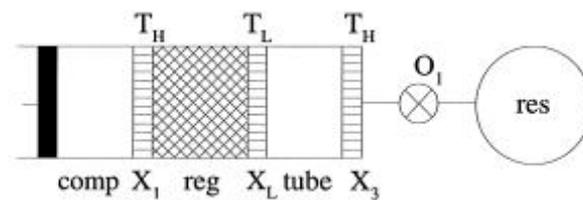
Figure 2.3 Schematic diagram of a Stirling-type single inlet pulse tube refrigerator.

The compressor generates a pressure *P* in the system which varies periodically in time. The cooling at the cold heat exchanger X_L takes place due to the fact that the gas leaves the heat exchanger to the right with a temperature T_L and comes back with a temperature lower than T_L. Typically, the pressures are in the 10-20 *bar* region. The pressure varies rather smoothly with time and usually the gas velocities are small.

2.3 Ti:sapphire laser

Ti:sapphire mode-locked lasers provide a large wavelength tuning range, from about 690 to over 1050 nanometers, with pulse widths approximately 100 femtoseconds in length. Note that the lowest pulse width attainable in the actual Spectra Physics laser is 50 femtoseconds. In addition, these lasers have sufficient power (greater than 100 milliwatts throughout the tuning range) for saturation of two-photon excitation in most fluorophores. To ensure proper cooling and humidity control of the laser crystal, nitrogen gas is pumped into the sealed laser head, which is maintained at constant temperature by an external chiller.

The Titanium trivalent cation is responsible for laser action in doped sapphire crystals, which are produced by introducing titanium oxide into a melt of aluminum oxide. In the melt, some of the titanium ions diffuse into the aluminum oxide and are incorporated into lattice positions in place of aluminum cations. When excited by the argon-ion pump laser, titanium atoms in doped sapphire crystals absorb the greenish-blue light, which is subsequently released as coherent infrared light via stimulated emission. As the emitted light is repeatedly reflected back through the crystal with mirrors, it is amplified until laser oscillation occurs. Ti:sapphire lasers require a supporting pump laser of sufficient power to excite the crystal and initiate laser action. Power requirements vary with output demand, but strongly focused argon-ion lasers having values between 5 and 20 watts can be utilized for this purpose. Recently, new solid state lasers have been developed that employ nonlinear conversion to double the output frequency of infrared lasers to produce lower wavelength green light. These lasers are far more efficient than argon-ion lasers and also have reduced power and cooling demands.

2.4 Streak camera

A Streak camera is an optoelectronic device used to observe light emission phenomena occurring on the sub-nanosecond time scale. Together with the TCSPC is one of the most widely used technique to record PL time decays.

Streak cameras building blocks are:

- Photocathode

- Streak tube

- Image recording device (CCD)

A scheme of the device with the main parts is illustrated in *Figure 2.4*. The operating principle can be explained considering a light pulse with a certain time profile *f(t)*. When the light impinges the photocathode a proportional amount of electrons is emitted and is accelerated across the streak tube. In the streak tube two parallel deflection plates are settled.
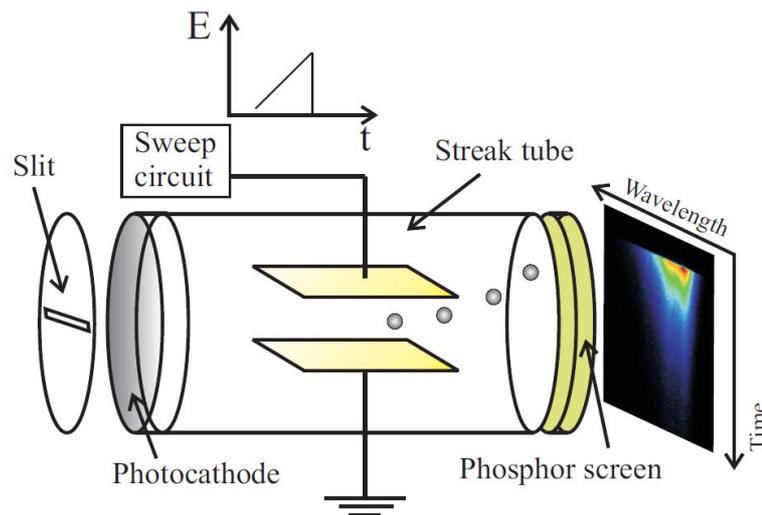
Figure 2.4 *Scheme of the streak camera. The slit selects the photons that impinge on the photocathode. The photocathode converts photons into electrons. Inside the streak tube two plates are used to deflect electrons according to the voltage ramp applied by the sweep circuit. The phosphor screen converts electron into photons. Photons are recorded with the CCD (not shown) placed after the phosphor screen.*

In synchrony with the arrival of electrons a rising voltage ramp is applied to the plates. Electrons that first enter the tube are deflected very little, since the value of the electric field (**E**) is low. Electrons which enter later are further deflected, because of the increased field. In this way the original light pulse *f(t)* is swept in space *f(y)* as a streak in the direction *y*, that is parallel to the electric field. At the tube end a phosphor screen converts electrons back to photons that are recorded as an image by

a CCD. The resulting data are obtained as an image in which the y axis represents time and *x* the wavelength if a spectrograph is coupled in front of the photocathode at the entrance slit. In the right part of *Figure 2.4*, a typical streak image with the PL intensity reported in false color it is shown. In our setup a spectrograph with three different gratings (50 *g/mm*, 100 *g/mm* and 1200 *g/mm*) is used to disperse the wavelength along the *x* axis before entering the horizontal slit. Spectral resolution for the three different gratings is: 17 *meV*, 10 *meV* and 0.8 *meV* respectively. In the Streak camera the arrival of light pulses and the sweep of the electric field must be synchronized with a trigger. The optical trigger used for this purpose is shown in figure 2.3 and consists of a fast PIN diode that drives the sweep circuit according to the Ti:sapphire repetition rate (~ 80 *MHz*). The temporal resolution of the streak camera employed in the setup of figure 1.3 is 1.9 *ps*. However, this is the so called one-shot resolution. The actual time resolution during signal integration is larger. In particular, the unremovable time jittering of the streak camera during integration is responsible for a time resolution of 5 ps. Exhaustive reviews on streak cameras can be found in references[59, 60].

2.2.1 Confocal Laser Scanning Microscopy (CLSM)

Conventional optical microscopy uses extended light sources to illuminate all the sample field of view at the same time to create a magnified image, viewed by eyes or by an extended detector. In confocal microscopy light from a point source probes a very small region and a point detector ensures that only light from the very same small area is detected. For this purpose a point detector must be located in a plane conjugated (confocality) with the point source. *Figure 2.5* shows a simplified scheme of the working principle of a confocal microscope. The spatial filter (*pinhole*) ensures that the detector is practically point-like. In the figure only the PL (colored lines) from the focal plane of the sample is focused on the detector (PMT4). Thus *confocal microscopy* is able to reject features that are out of focus. Confocal microscopy has two main advantages with respect to conventional microscopy:
- Optical sectioning and 3-D reconstruction of translucent specimens.
- In plane spatial resolution increased by a factor 1.4[61].

Spatial resolution is one of the most desired features of every microscope. The resolution can be measured or calculated considering the *FWHM* of the image of a sub-resolved point object. This image is usually called pointspread function (PSF).
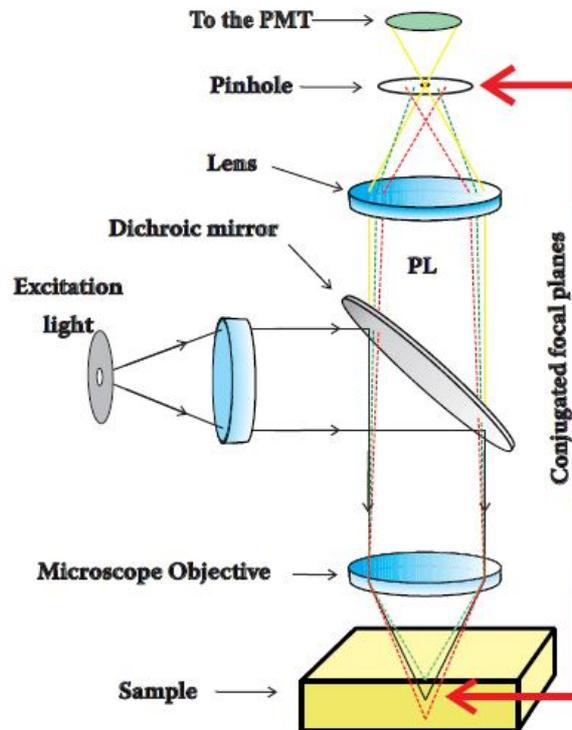
Figure 2.5 *Schematic diagram illustrating the operation principle of a confocal microscope. The excitation light is reflected by a dichroic mirror and focused by the objective, the sample PL (colored lines) is recollected by the objective and focused on the pinhole that prevents the out of focus PL rays (dotted lines) to reach the detector.*

Table 2.1 lists the spatial in plane (*x-y*) and axial (*z*) resolution for different optical microscopy techniques. Note that resolution is expressed as a function of the wavelength of light, considering an objective with NA = 1.4 for the far field techniques (i.e. Optical and Confocal microscopy) and a pinhole of null size for the confocal microscope. The resolution values reported in *table 2.1* refer to the case in which light of the same wavelength λ is used to illuminate the sample and to reconstruct the optical image. When the light arising from PL is detected, two different wavelength are involved in the process of image formation: λ_1 is used to excite the sample and λ_2 is the longer PL wavelength used to form the image. In order to take this into account, values reported in table 2.1 for confocal microscopy are linearly dependent on a factor β that is defined as $\beta = \lambda_2/\lambda_1$. Even if it is practically impossible to work with $\beta = 1$, this value represents the ideal limit once the exciting wavelength λ_1 is fixed.

	Optical Microscopy	Confocal Microscopy
x-y resolution	0.436λ	0.31λ
z resolution	2λ	0.46λ

Table 2.1 In plane (x-y) and axial (z) resolution for conventional optical microscopy and confocal microscopy.

Since in *confocal* microscopy only a diffraction limited point is imaged, the sample or the light must be scanned in order to obtain an image of the desired field of view. It has been demonstrated that sample scanning confocal microscopy has a better resolution than laser scanning[62]. However, the latter allows obtaining fast imaging without sample degradation ad has found a wider diffusion in commercial instruments. The scan of the exciting laser beam can be accomplished with scanning galvanometric mirrors. In *Figure 2.6* a schematic drawing of a scanning head for confocal microscopy is shown. The exciting laser beam is illustrated as a continuous line and is scanned by two galvanometric mirrors. PL is represented by the dotted line. The confocal PL image of the studied sample is reconstructed by the microscope software, collecting the PL point by point.
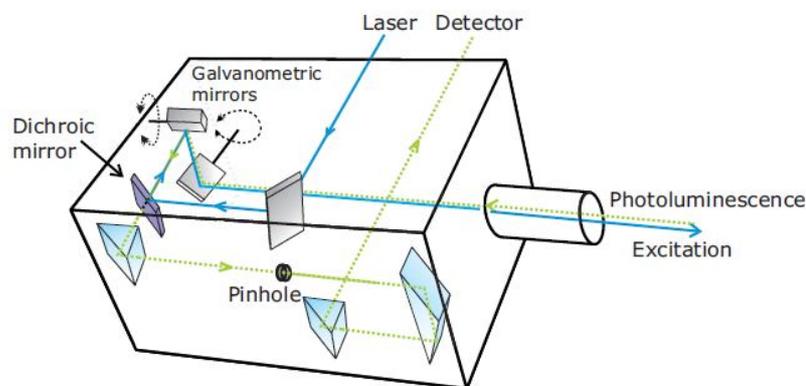
Figure 2.6 Schematic drawing of a laser scanning head: Excitation laser beam (continuous line) is reflected by the dichroic mirror and is scanned on the sample surface by the galvanometric mirrors. PL is collected through the same optical path, it passes the dichroic mirror, the pinhole and reaches the detector

2.2.2 Atomic Force Microscopy

Atomic force microscopy (AFM) belongs to the family of the Scanning Probe Microscopy (SPM) techniques. SPM are based on 3-D scanning of a sample surface, through a probe which locally interacts with the surface[63, 64] . The probe is placed near the surface (d < 100 *nm*). An electronic system measures the surfaceprobe interaction at every (x,y) point in the sample[65] . The probe is moved on top of the sample by a piezoelectric actuator, in order to cover a path called raster. The interaction strength (whatever its nature is, depending on the SPM techniques) depends on the sample-probe distance. By mapping the strength in the (x,y) points, we could obtain an image of the sample surface. AFM was invented by G. Binning, C. Gerber and C. Quate[66] . It overcomes the limits of other SPM (like Scanning Tunneling Microscopy, STM) because it permits the analysis of all type of samples (insulator, semiconductor, etc). Furthermore, it allows processing in air, vacuum or liquid environment[67–70].The main components of an AFM are schematically showed in *Figure 2.7*

• The different interactions (magnetic, electric, etc) settled between the surface and the probe are strictly dependent on the nature of the probe itself.

• The piezoelectric transducer (also called scanner) which permits probe or sample movements. Movements are possible in all the three spatial directions with an accuracy in the order of $10{-}12$ *m*. Vertical movements are guided by a feedback system which keeps the surface-probe interaction fixed. These movements are recorded and used to determine the topological profile of the surface.
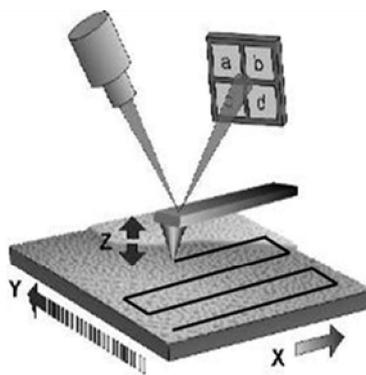
Figure 2.7 *Scheme of the working principle of the AFM. The scanner moves the sample thereby changing the tip/surface interaction and the optical path of the laser beam, whose movement is collected by a photo-diode.*

• An electronic system used to measure and to amplify the probe-surface interaction.

• A mechanical system, to damp the external vibrations; the above mentioned feedback system for keeping the signal with the physical information at a set value (setpoint).

• A control system for the acquisition and visualization of the data.

In the AFM technique, the probe is a very sharp pyramidal or conical tip fabricated on the edge of a lever called cantilever. When the tip and the surface interact, a force modifies the cantilevers mechanical balance. These change is detected by a laser beam focused on the back of the cantilever (*Figure 2.7*). The laser beam, after a convenient optical path, reaches a sensor (beam and bounce). During the surface scanning, the sensor (usually a photo-diode) reveals the different laser beam positions that, after a suitable amplification, are used to reproduce the surface topography.
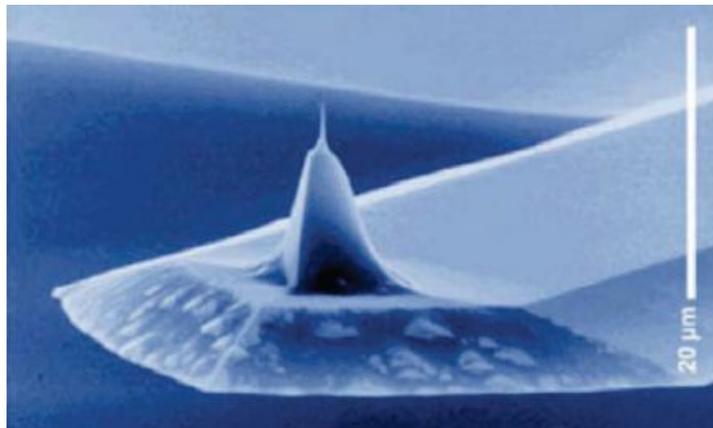
Figure 2.8: *Scanning electron micrograph of a micromachined silicon cantilever with an integrated tip pointing in the [001] crystal direction (Wolter et al., 1991).*

The probe is the fundamental part of the instrument since it sets the minimal spatial resolution of the AFM. Ideally, it is conceived to be sensitive to a single chemical-physical interaction with the surface. But in practice this in not possible, so fabrication is important to minimize parasite interactions. There are rectangular or triangular shape levers with conic or pyramidal tip. Classic conic tips present these features: length around $100 - 130\mu m$, $35\mu m$ wideness, $2\mu m$ thickness, tip radius of curvature of 10 *nm* and an elastic constant less than 10 *N/m Figure 2.8*. Several forces typically contribute to the deflection of an AFM cantilever. The force most commonly associated with atomic force microscopy is an interatomic force called the van der Waals force. The dependence of the van der Waals force upon the distance between the tip and the sample is shown in *Figure 2.9*

Two distance regimes are labeled on *Figure 2.9*: (*i*) the contact regime; and (*ii*) the non-contact regime. In the contact regime, the cantilever is held less than a few angstroms from the sample surface, and the inter-atomic force between the cantilever and the sample is repulsive. In the non-contact regime, the cantilever is held on the order of tens to hundreds of angstroms from the sample surface, and the inter-atomic force between the cantilever and sample is attractive (largely a result of the long-range van der Waals interactions).
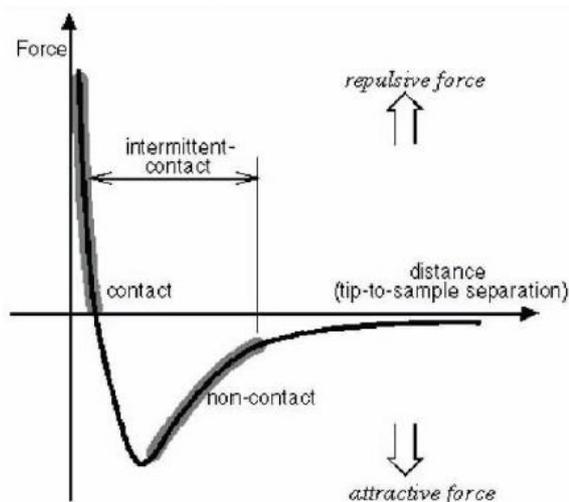
Figure 2.9 *Graph showing the repulsive/attractive forces between the surface and the cantilever as a function of the distance.*

A third operation mode has been developed, between the contact and non contact modes: the semi-contact or tapping Mode (*Figure 2.10*). In Tapping Mode AFM the cantilever is oscillated at or near its resonance frequency with an amplitude ranging typically from 20 to 100 *nm*. During the scan the tip lightly *taps* on the sample surface contacting the surface at the bottom of its swing[71, 72]. The feedback loop keeps constant the oscillation amplitude by maintaining a constant root-mean-mean value of the oscillation signal acquired by the split photodiode detector (setpoint).

Figure 2.10: *Scheme of the AFM working modalities. In contact mode the topography is obtained by the cantilever bending; in no- contact mode and semi-contact (or tapping) mode the signal comes from the variation of frequency, magnitude and phase of the cantilever oscillation.*

Then the vertical position of the scanner at each (x,y) data point is stored by the computer to form the topographic image of the sample surface. Clearly in this scanning modality a constant tip-sample interaction is maintained during imaging since a constant oscillation amplitude is maintained. Operation can take place both in ambient and liquid environments. When imaging in air, the typical amplitude of the oscillation allows the tip to contact the surface through the adsorbed fluid layer without getting stuck. The advantages of this procedure are low sample damaging and good lateral resolution. The semi-contact mode is usually employed for soft and biological materials.

2.3 Thin Films growth by vacuum sublimation

In this section the processing technique that we have used to grow thin films of T4DIM will be illustrated. After a brief introduction about the physical principles of vacuum sublimation, a detailed description of the two evaporation systems for UHV and HV in our laboratory will be provided.

Introduction to vacuum sublimation

Vacuum sublimation has experienced an enormous diffusion in the last decades as a technique to prepare thin films of small molecule organic semiconductor[73]. The main advantage of this technique consists of providing a sub-monolayer thickness control during the growth. Moreover, the ultraclean environment provided by the vacuum ensures a low level of contamination, due to moisture or chemical impurities. The core of every evaporator consists of a vacuum chamber with a crucible and a substrate held perpendicularly to the crucible orifice. In *Figure 2.11* a scheme of a common vacuum chamber is shown. Once the crucible is filled with the purified material, it is heated until it reaches the sublimation temperature of the material. The material exits the crucible orifice as a molecular beam and impinges on the substrate.
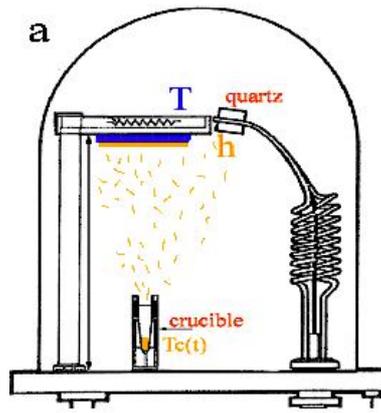
Figure 2.11 *Scheme of a vacuum chamber for sublimation of organic materials. At the bottom of the chamber is represented the crucible filled with the organic material. On top, the substrate holder and the quartz microbalance are placed in correspondence to the crucible orifice.*

Then, according to the substrate temperature, the molecules can be adsorbed, desorbed or diffuse to a nucleation center. Consequently, the substrate temperature is a crucial variable to modulate the growth of thin films with different morphologies[52]. The quartz crystal oscillator placed near the substrate is used to monitor the amount of material deposited. Thus evaporation rate and the film nominal thickness can be easily calculated after an accurate calibration procedure. The two main variables to play with, in order to have different regimes of growth and consequently film morphologies, are the substrate temperature and the deposition rate. The former can be controlled with a resistance attached to the substrate holder while the latter depends on the crucible temperature. Setups In the UHV setup the very low base pressure (10^{-8} *Pa*) permits to grow thin films in an ultraclean environment in a regime of molecular beams (OMBD). During growth the pressure is ($\sim 5 \cdot 10^{-7}$ *Pa*). This level of vacuum can be achieved with the combination of a turbomolecular and a cryo-pump. The substrate is placed at about 30 *cm* from the crucible that is a Knudsen cell. Substrate temperature can be varied in the range ($-200 \div 1000$) $^{\circ}$C. Six different cells are present at the bottom of the chamber in order to grow different materials and to have also the possibility to grow hetero-structures or to co-evaporate. Every cell is equipped with a mechanical shutter in order to start and stop the growth process instantaneously. Before and after the growth, cells are maintained few degrees under the sublimation temperature in order to constantly outgassing the source materials from impurities.

The HV setup has a base pressure of (10^{-6} *Pa*) thanks to a turbomolecular pump. In this setup the substrate is placed at about 20 *cm* from the crucible. Temperature of

the substrate holder can be varied in the same range of the temperature of the UHV setup.

Purification of T4DIM

The chemical purity of organic materials is a crucial issue both for applications and for fundamental studies. In fact, chemical impurities can scatter charge carriers or trap excitons. Thus, a well performed purification procedure is necessary for any reliable experiment on organic semiconductor. **T4DIM** was purified with two cycles of sublimation on a water cooled finger. Before putting the material into the vacuum chambers purity level has been checked by mass-spectrometry.

2.3.2 Device fabrication

Two Organic Light Emitting Transistor (OLET) were fabricated in bottom gate-top contact geometry. The ITO substrates cleaning procedure consist of two sonication cycles, in acetone first and 2-isopropanol then, for 10 minutes each. The 450 *nm* thick dielectric layers of PMMA have been grown by spin-coating on top of the clean ITO substrate (relative electric permittivity ε = 3.6 at 100 *Hz*). The PMMA film were then thermally annealed in a glove box at 120°C (around 10°C above the glass transition temperature for PMMA) for 15 hours under inert atmosphere. (C PMMA = 7.08 *nF/cm^2*). The 30 *nm* thick layers of **T4DIM** have been grown by vacuum sublimation in a home-made vacuum chamber, with a deposition rate of 0.1 *Å/s* and 0.01 *Å/s* at a base pressure of 10 $^{-6}$ *mbar*. The substrate temperature during the film deposition has been kept at room temperature (RT). The drain-source electrodes were made of gold and were evaporated through a shadow mask on top of the organic thin films. The gold layer thickness is 50 *nm*, while the channel length and the channel width are 70 *μm* and 15 *mm*, respectively. All opto-electronic measurements were carried out in an MBraun nitrogen glove box using a standard SUSS Probe Station equipped with a Hamamatsu photodiode for light detection. The mobility values in saturation regime are calculated from the locus curves using the standard equations [Eq 4].

References

[54] J. N. Demas and G. A. Crosby, The Measurement of Photoluminescence Quantum Yields. A Review, The Journal of Physical Chemistry (**1971**), 75, 991.

[55] J. C. de Mello, H. F. Wittmann, and R. H. Friend, An Improved Experimental Determination of External Photoluminescence Quantum Efficiency, *Advanced Materials* (**1997**), 9, 230.

[56] J. W. T. Walsh, Photometry, Constable, London 1953.

[57] Y. Matsubara, Proceedings of the 17th International Cryogenic Engineering Conference, Institute of Physics, 1998, p. 11.

[58] W. Demtroder, Laser *Spectroscopy: Basic Concepts and Instrumentation 3rd Ed.* Berlin: Springer-Verlag, **2003**.

[59] J. R. Lakowicz, *Topics in Fluorescence Spectroscopy, Volume 1: Techniques.* New York: Plenum Press, **1991**.

[60] A. J. Campillo and S. L. Shapiro, "*Picosecond streak camera fluorometry a review*," IEEE J. quant. elec., vol. 19, pp. 585–610, **1983**.

[61] T. Wilson, Confocal Microscopy. London: Academic Press, **1990**.

[62] J. B. Pawley, Handbook of biological Confocal Microscopy. New York and London: Plenum Press, **1990**.

[63] O. Marti, H.O. Ribi, B. Drake, T.R. Albrecht, C.F. Quate, and P.K. Hansma. Atomic force microscopy of an organic monolayer. *Science*, 239(4835):*50–52*, **1988**.

[64] C.B. Prater, H.J. Butt, and P.K. Hansma. Atomic force microscopy. *Nature*, 345(6278):*839–840*, **1990**.

[65] J.B. Pethica and W.C. Oliver. Tip surface interactions in stm and afm. *Physica Scripta*, T19A:*61–66*, **1987**.

[66] G. Binning, C.F. Quate, and C. Gerber. Atomic force microscope. *Phys. Rev. Lett.*, 56:930, **1986**.

[67] O. Marti, B. Drake, and P.K. Hansma. Atomic force microscopy of liquid-covered surface - atomic resolution images. *Appl. Phys. Lett.,*

[68] T.R. Albrecht and C.F. Quate. Atomic resolution imaging of a nonoconductor by atomic force microscopy. *J. Appl. Phys.*, 62(7):*2599–2602*, **1987**.

[69] M.D. Kirk, T.R. Albrecht, and C.F. Quate. Low-temperature atomic force microscopy. *Rev. Sci. Instrum.*, 59(6):*833–835*, **1988**.

[70] C.M. Mate, M.R. Lorenz, and V.J. Novotny. Atomic force microscopy of polymeric liquid-films. *J. Chem. Phys.*, 90(12):*7550–7555*, **1989**.

[71] C.B. Prater and Y.E. Strausser. *Tapping Mode Atomic-Force Microscopy – Applications to Semiconductors*. Intitute of Physics Conference Series, **1994**.

[72] P.K. Hansma, J.P. Cleveland, M. Radmacher, D.A. Walters, P.E. Hillner, M. Bezanilla, M. Fritz, D. Vie, H.G. Hansma, C.B. Prater, J. Massie, L. Fukunaga, J. Gurley, and V. Elings. Tapping mode atomic-force microscopy in liquids. *Appl. Phys. Lett.*, 64(13):*1738–1740*, **1994**.

[73] S. R. Forrest, "Ultrathin organic films grown by organic molecular beam deposition and related techniques," Chem. Rev., vol. 97, pp. 1793–1896, **1997**.

Chapter 3

Synthesis and Optical properties in solution of T4DIM

In this chapter, we show the synthetic route and its optical properties in solution of the novel semiconductor compound that is the focus of this thesis. In particular, we analyze how the polarity of the solvent and the solution concentration influence both the steady-state absorption and emission spectra. We also carry out time-resolved photoluminescence spectroscopy supported by a theoretical analysis, in order to understand the dynamics of the spectral relaxation.

3.1 Introduction

The properties of aromatic imides are strongly dependent on their π-conjugated cores. For example, anthracene diimide derivatives (**ADI**s) display n-type transport properties[74] when implemented as active material in thin-film organic transistor. In contrast, linear dibenzotetrathiafulvalene diimide derivatives (**DBTTFDIs**, *Figure 3.1*) exhibit hole transport characteristics[75]. Until now, aromatic imide studies are primarily focused on fused phenyl imides, such as naphthalene[76] and perylene diimides[77] (**NDIs** and **PDIs** respectively). To further understand the relationship between molecular structure and functional properties, it is necessary to synthesize novel types of aromatic imides with differently π-conjugated cores. Thiophene-containing compounds are frequently used in organic electronics[78]. Among these molecules, linear ring-fused thiophenes have attracted particular attention because they exhibit rigid structures, strong intermolecular interactions, and usually high device performances[79]. Recently, several groups have reported the high power conversion efficiencies of *thieno[3,4-c]pyrrole- 4,6-dione-based* (**TPDO**) copolymers in solar cells[80].
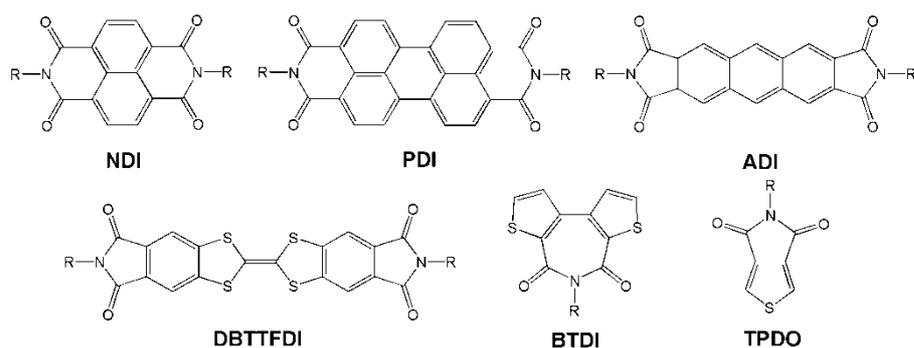
Figure 3.1 Chemical Structures of Some Aromatic Imides

Facchetti et al. discovered that *N-alkyl-2,2-bithiophene- 3,30-dicarboximides* (**BTDI**) is an ideal π-conjugated units for the construction of electron-transporting organic semiconductors[81]. All of these results suggest that thiophene-based imides may implement fruitfully in organic electronics. In this direction, fully fused linear oligomers based on a dithienothiophene-diimide block were also described, showing low-laying LUMO energy levels and close intermolecular packing distance[82]. However, the locked structure of such systems could limit their chemical diversity, with consequent narrow accessibility to fine-tuning optoelectronic and morphologic properties.

We recently reported a new oligothiophene molecu bearing thienopyrrolyl dione symmetric ends *(2,20-(2,20-bithiophene-5,50-diyl)bis(5-butyl-5H-thieno[2,3-c]pyrrole-4,6)-dione*, (**T4DIM** *Figure 3.2*). This compound exhibits reduced energy band gap with ambipolar electrical behavior and electroluminescence in single-layer OLET device architecture[83].
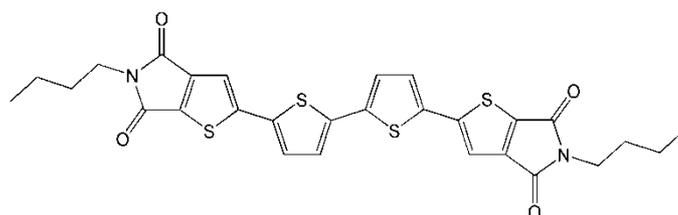
Figure 3.2 Molecular Structure of **T4DIM**

3.2 Synthesis of T4DIM

The linear multistep synthetic sequence to **1** starts from thienopyrrolyl dione **7** that is readily available through a variant of a known protocol[84] (*Figure 3.3*).
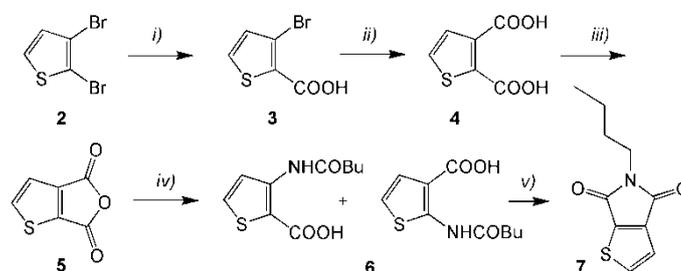
Figure 3.3 *Synthetic route to key thienopyrrolyl building block **3**. i) BuLi, CO_2 gas, Et_2O, ii) acetic anhydride, reflux, iii) buthylamine, toluene, reflux, iv) $SOCl_2$, reflux.*

Then, Stille cross-coupling with tributylstannylthiophene **9** and bromo derivative **8** led to the dimer **10** in satisfactory yield (75%), which was then brominated under conventional halogenation reaction. Finally, microwave (MW)[85]-assisted (P = 300 W, T = 80 1C, 10 min) high throughput, high purity borylation/Suzuki coupling[86] ($PdCl_2$ dppf, 5 mol%) followed by simple reaction work-up provided 1 in 79% isolated yield. For comparison compound **1** was also available through Stille coupling, however, time-consuming repeated purification steps were required.
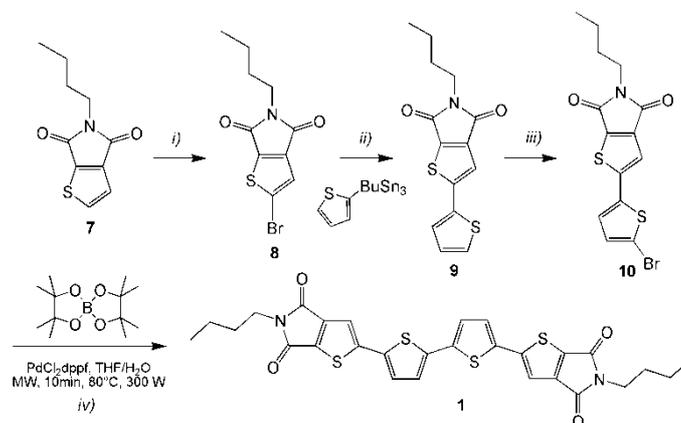
Figure 3.4 *Synthetic route to T4DIM. (i) NBS, TFA, H_2SO_4, (ii) Stille coupling, (iii) NBS, DCM/acetic acid, (iv) one-pot borylation/Suzuki coupling under MW assistance.*

The chemical structures of all compounds are supported by characterization, such as ^{1}H-NMR, MS and elemental analysis at the of this thesis.

3.3 Linear optical properties of T4DIM in solution

3.3.1 Steady-states absorption ad emission of T4DIM in solutions

Absorption

The absorptions spectra at room temperature of **T4DIM** were recorder in various solvents ranging from non-polar mixture eptane-tuluene (*9:1*) to polar DMSO *(Figure 3.4a)*. Regardless the solvents, the absorption spectrum consists in a strong band in the *400–500 nm* together with a shoulder of this band in the *350–375 nm* region. Both bands are broad and unstructured moreover are clearly dependent on the solvent polarity. In fact, the maximum absorption wavelengths red-shift with the increasing polarity of the solvent (*Table 3.1*). However, the solvatochromic shift is rather small (*~20 nm* in DMSO compared to *eptane-toluene* case), which indicates a small difference between the dipole moments of the Franck–Condon (FC) excited state and the ground state. The absorption properties of T4DIM also show drastic changes on presence of added acid (*Figure 3.4b*). With decrease in pH of the solution, the absorption intensity of *450 nm* band decreases with a bathocromic shift to *475 nm*. whereas concomitant slight increase of absorption band at *365 nm* is present.
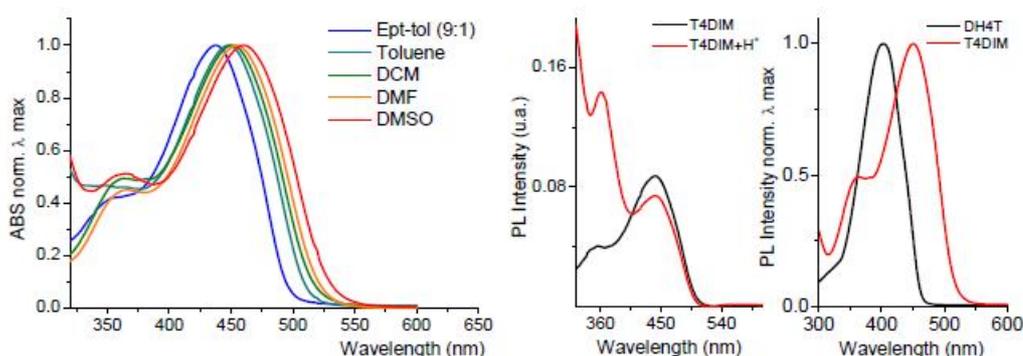
Figure 3.4 *(a) Normalized absorption spectra of T4DIM in different solvents ($10^{-6}M$); (b) pH effect on absorption spectra of T4DIM (left); Comparison of the absorption maximum between dihexyl substituted sexithiophene DH4T and T4DIM (right).*

This result is deeply correlated with the particular structrure of T4DIM. In fact, the carboxylic imide groups are stabilized in resonance due to the electron pair of nitrogen, that is partly delocalized over the carbonyl groups. Addition of an acid (*HCl in diethyetere*) to the neat solution generates a H^+ reaction with the non-

bonding electrons of carboxylic imides group of T4DIM. The protonation of the carbonyl oxygen atoms is expected rather than the addition of the proton onto nitrogen, because the stabilization in resonance energy would be lost otherwise. Generally when a group playing the role of an electron donor in the fluorophore interacts with a cation, the latter reduces the electron-donating character of this group; owing to the resulting reduction of conjugation, a blue shift of the absorption spectrum is expected together with a decrease of the extinction coefficient. Conversely, a cation interacting with the acceptor group enhances the electron-withdrawing character of this group; the absorption spectrum is thus red-shifted and the molar absorption coefficient is increased. (*Figure 3.5*).
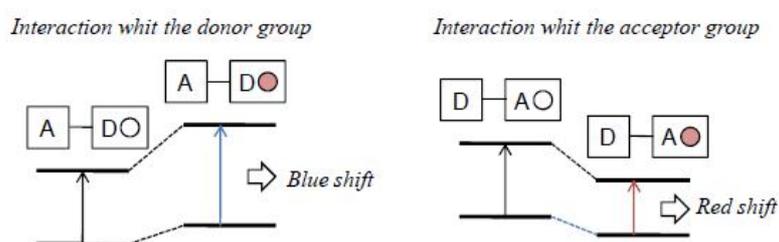
Figure 3.5 *Spectral displacements of emitting molecule resulting from interaction of a bound cation with an electron-donating or electron-withdrawing group.*

Respect to the homologous alkyl-chain thiophene derivatives, it is interesting to estimate how the energy gap E_g depends on the structural modifications introduced in T4DIM. A comparison of the absorption maximum between dihexyl substituted quaterthiophene (DH4T) and **T4DIM** dissolved in the same solvent is shown in *Figure 3.4b.* The main peak of DH4T is blue shifted by *50 nm* compared to T4DIM. This result is due to the higher conjugation length originated by the inclusion of the pyrrolydinone moieties in the conjugated system. Indeed, the absorption spectral region of T4DIM results close to the that of *dihexyl substituted sexithiophene* (λ_{max} = 440 nm)[87] in which the conjugation length was extended over six thiophene units.

Solvent	ε_r (25°C)	Abs(*nm*)	
Ept-Tol	1.92	335	437
Toluene	2.38	356	447
DCM	8.93	362	450
DMF	36.71	364	454
DMSO	46.68	362	459

Table 3.1 *Steady-state Absorption data of T4DIM in different organic solvent*

It is important to note that the same spectral profile was obtained at concentrations from 10^{-6} to 10^{-3} mol·dm^{-3} in all solvents, with linear dependence of absorption upon concentration. The linear nature of the of the Lambert – Beer law suggests that the aggregation phenomena are not significant in these range of concentrations.

For example in *Thiacarbocyanine*[88] (TCC) the absorption spectrum of the 10^{-6} M solution comes from the TCC monomer. As the concentration of the dye increases up to *10^{-3}M* the spectrum exhibits a relatively blue shift curve in comparison to the monomer spectrum. This blue shifted spectrum is commonly assigned to H aggregates. When the concentration is further increased a sharp and intense band which is red-shifted with respect to the monomer peak appears for concentration higher than *3×10^{-3}M*. In our case the absorption characterization of T4DIM with varying concentration did not show bathocromic or hypsocromic shift of the main peak, moreover no absorbance degradation of the solutions was observed after storage ambient condition for one week, indicating the high environmental stability of this compound.

Fluorescence

The steady-state fluorescence spectra collected for the same solutions reported above are shown in *Figure 3.6a*. Using a mixture of eptane-toluene as solvent the emission profile of T4DIM results structured with at least 3 vibronic peaks clearly visible. The emission maximum wavelength is around *500 nm*. However, with increasing solvent polarity, the emission becomes structureless and the peak position shows a significant red-shift. Together with the large solvatochromic shift of the fluorescence spectra, also fluorescence quantum yields decrease with increasing solvent polarity. Indeed, the fluorescence efficiency was reduced by factor of 3 varying the solvents from the eptane-toluene to DMSO (*Table 3.2*)
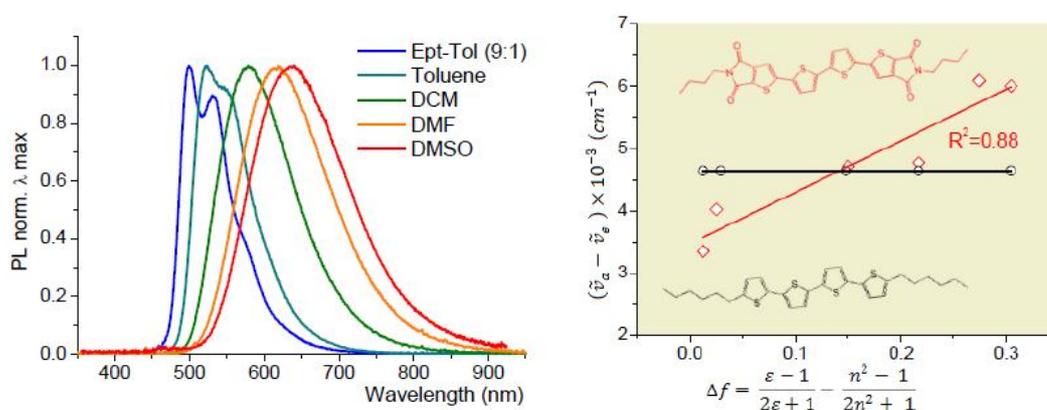
Figure 3.6 *(a)Normalized emission profiles (exc. wavelength 442nm) for T4DIM in different organic solvents (10^{-6}M); (b)Lippert Plots for DH4T and T4DIM.*

Solvent	Emis.(*nm*)	*Stokes (nm)*	Φ_f
Ept-Tol	498	61	0.15
Toluene	521	74	0.12
DCM	580	130	0.08
DMF	617	163	0.06
DMSO	636	177	0.045

Table 3.2 *Steady-state fluorescence data of T4DIM in different organic solvent. Quantum yield measurement were performed with an integrating sphere (Laser excitation wavelength 442 nm).*

This result suggests a large rearrangement of the charge density in the excited states between the Frank-Condon excited state and the emissive one. In fact, the higher sensitivity to the solvent polarity is probably a signature of the charge transfer in excited states from the electron donor, towards the electron acceptor. In T4DIM molecule both groups are presents, since two strong electron-withdrawing diimide

groups have been symmetrically introduced in between the electron-donating oligothiophene π core. Thus, the dipole moment interacts with the polar solvent molecules to reduce the energy of the excited state. The steady-state solvatochromism can be qualitatively explained by simple model of a linear dipole in a dielectric continuum. The relation between the Stokes shift and the solvent polarity is usually given by Lippert-Mataga equation[89].

$$\upsilon_{abs} - \upsilon_{fl} = \frac{2|\Delta\mu|^2}{hca^3}\left(\frac{D_s - 1}{2D_s + 1} - \frac{n^2 - 1}{2n^2 + 1}\right)$$

where υ_{abs} and υ_{fl} denote energy corresponding to the absorption and the emission maxima, wavelength respectively. $|\Delta\mu|$ is the magnitude of the difference in dipole moments between the ground and the excited states and a is the radius of a spherical cavity containing the dipole. The term in the bracket is called the orientation polarizability Δf and depends on the dielectric constant D_S and optical refractive index n of the solvent implemented in the measurements. In *Figure 3.6b* the representative *Lippert-Mataga* plots for T4DIM in comparison with (DH4T) are shown. The experimental data are well-interpolated by a straight line for both compounds. As aspect for the DH4T the constant value of the Stokes shift with respect the medium polarizability indicates that no charge separation occurs during the excitation.

Differently, in the case of T4DIM the slope of the interpolating line can represent the difference in transition dipole moment between the ground and excited states. It is interesting to note that the linear dependence from the polarity in T4DIM indicates that the fluorescence spectrum consists mainly of one band. This feature is not present in other compounds in which an ICT process occur. For example in 4-(N,N-dimethylamino)benzonitrile (DMABN)[90] or in 6-(phenylamino)-2-naphthalenesulfonate (6,2-ANS),[91] since two straight lines with different slopes are necessary to fit the data. Indeed, in the case of 6,2-ANS this experimental result can be correlated to the presence of emission bands from two distinct excited states with different charge distributions.

From the emission spectrum of DMABN in polar solvent, it possible to establish both *local excited* (LE) and *internal charge transfer fluorescence* (ICT). The origin of the dual fluorescence observed first in DMABN and later in a large number of electron donor-acceptor compounds can be exemplified by the energy the surface diagram shown in *Figure 3*.6. The LE-ICT reaction is referred to as a reversible

process in which k_a and k_d are respectively the rate constant of the forward and backforward intramolecular charge transfer.
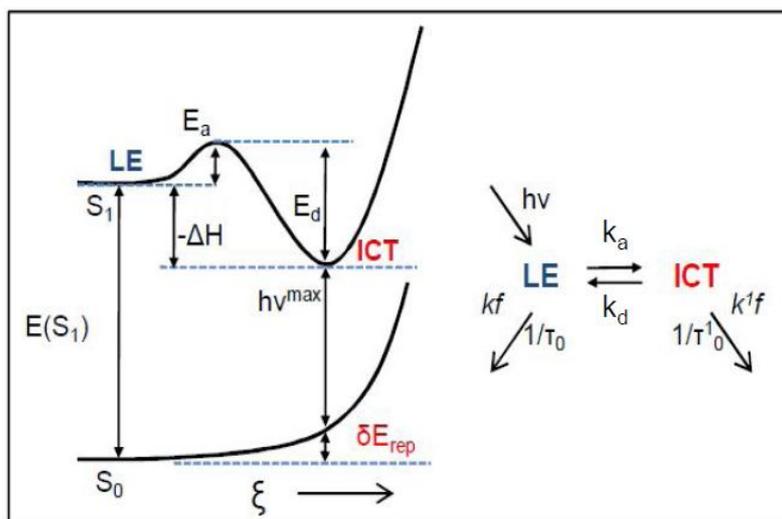
Figure 3.6 *Potential energy diagram for ICT process. $E(S_1)$ is the energy of the S_1 state, E_a and E_d are the activation energies of the ICT reaction rate constants k_a and k_d. The value $-\Delta H$ is the difference in enthalpy between the LE and ICT states and $h\nu^{max}$ is the energy of the maximum of the ICT fluorescence band. δE_{rep} is the energy that determines the red shift of the ICT emission.*

The Frank-Condon (FC) state reached upon emission from the exciplex is stabilized with respect to the equilibrated pair (A-D) of ground state molecules by repulsion energy δE_{rep}. The difference between this value and $-\Delta H$ determines the red shift of ICT emission. It is clear that the ICT emission of DMABN and related molecules can easily be identified in the fluorescence spectrum by the large value of the repulsion energy δE_{rep}. In molecules for which δE_{rep} is small, it is difficult to establish from an analysis of the fluorescence spectrum whether such a compound is dual fluorescent or not. Typically, the magnitude of the ground state repulsion energy $\delta E_{rep}(CT)$ reflects the configurational changes that have occurred in the molecule DMABN and its immediate solvent environment during the ICT reaction from the S_0 ground state to the equilibrated ICT state. Two contributions to $\delta E_{rep}(CT)$ can be distinguished in principle: firstly, the reorganization of the solvent molecules, induced by the increase in the dipole moment; secondly, changes in the molecular configuration such as bond lengths and bond angles, due to the increase in charge separation when going from S_0 to CT.

3.2 Time Resolved Spectroscopy

In the previous paragraph we described the effects of solvent and local environment on the steady-state emission spectra. Given the evident solvatochromic effect, we showed that T4DIM is likely display internal charge transfer in the excited state. During the descriptions we did not consider the rate constants for this processes, but mostly assumed the lifetime of the compound was in equilibrium with its environment prior to emission. Time-dependent effects are not observed in the steady-state emission spectra, but can be investigated implementing time-resolved photoluminescence measurements in function of the emission wavelength. Here, I investigated how the spectral emission display time-dependent changes in the ps temporal range due to the influence of the polarity and viscosity of the solvent on ICT process. The setup used to perform time-resolved fluorescence lifetime measurements is described previously. Given the temporal decay range of the investigated, in the next reported fluorescence time decay profile the instrumental response function at *442 nm* excitation wavelength can be considered that are typically *30 ps* full with at half-maximum.

In non-polar solvent such as *Ept-Tol (9:1)*, *Toluene*, the PL lifetime constants decrease monotonically as the dielectric constant of the solvent increases (*Table 3.3*). In the case of polar aprotic solvents (such as DMSO) a bi-exponential interpolating curve are used to reproduce PL experimental decays and intense spectral dynamics is observed on the blue edge of the emission. Indeed, after the laser excitation, the emission spectra profile displays modulation during the first *75 ps*, then remaining unaltered with respect to the steady-state spectrum afterwards (*Figure 3.7*).

Solvent	Time (ns)
Ept-Tol	0.745
Toluene	0.705
DCM	0.590
Acetonitrile	0.585
DMSO	0.640
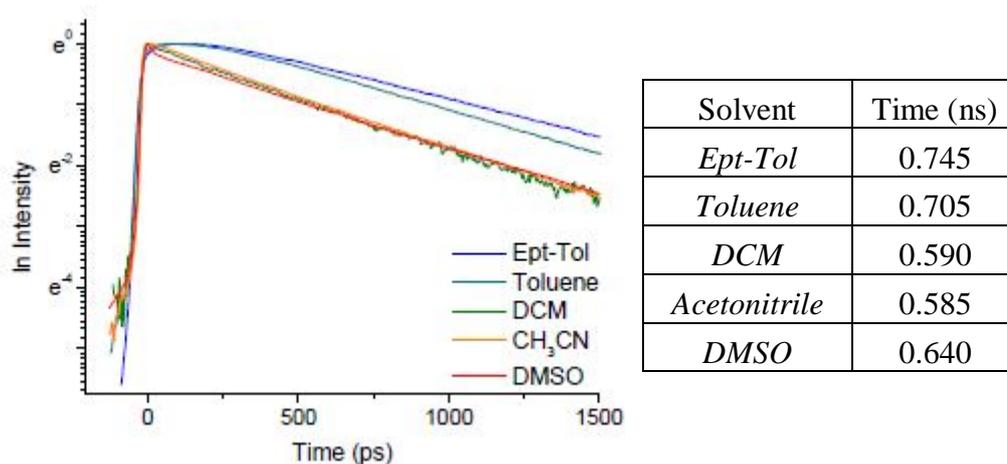
Figure3.7 *Fluorescence decays times of T4DIM in selected solvents spanning a range of polarities.*

As inferred from the steady-state investigation, this observation is in accord with a two-state model, consisting of an LE and ICT states. In particular, time-resolved fluorescence reveals that in T4DIM no dual emission and ICT is observed, even not in strongly polar solvent such as DMSO. The single exponential decay detected in ept-toluene or toluene solution indicates that the emission occurs from one distinct state, which is LE state at least in the time resolution limit of our setup. Then a fast switching of the fluorescence between the two possible states was observed only in DMSO solution, although the solvent dielectric constant is not much higher compared with acetonitrile.

To better understand the dynamics of photophysical processes taking place in the excited-state when polar solvents are implemented, we also analyzed the decay profiles with a higher temporal resolution (*6 ps*). Since acetonitrile and dimethylsulfoxide present nearly the same dielectric constant, true effects on the due internal charge transfer dynamics due to solvent viscosity might be observed in comparing these solvents. In *Figure 3.8* the black line shows the intensity decay of the total emission, while the other decay profiles are related to different wavelength ranges. The selected spectral ranges were chosen in order to follow the population kinetics of LE state and ICT state separately. As expected, also in acetonitrile solution we observed the dynamics due to an internal charge transfer but with faster dynamics with respect to DMSO (*Table 3.4*). In both cases the intensity decay, measured on the short-wavelength side of the fluorescence is more rapid than the decay of the total emission, because in this spectral region the LE state is decaying by both radiative and by the ICT processes.

Moreover, by comparison the time-resolved emission profile, when the solvent is changed from the fluid acetonitrile to viscous dimethylsulfoxide, it is interesting to note that, as time was passing by, the ICT emission in dmso solution is shifted to longer wavelength. Immediately after the charge transfer process indeed, the solvent molecules reorient around the excited fluorophore which is in the ICT state, that occurs with a solvent relaxation rate. Then a stabilization of this state determine a red shift of the emission while maintaining unaltered both the profile and width of the band. In less viscous solvents such as acetonitrile, the solvent relaxation dynamics is faster than the emission process from the ICT state, so that the red-shift with increasing time after excitation is not clearly visible.
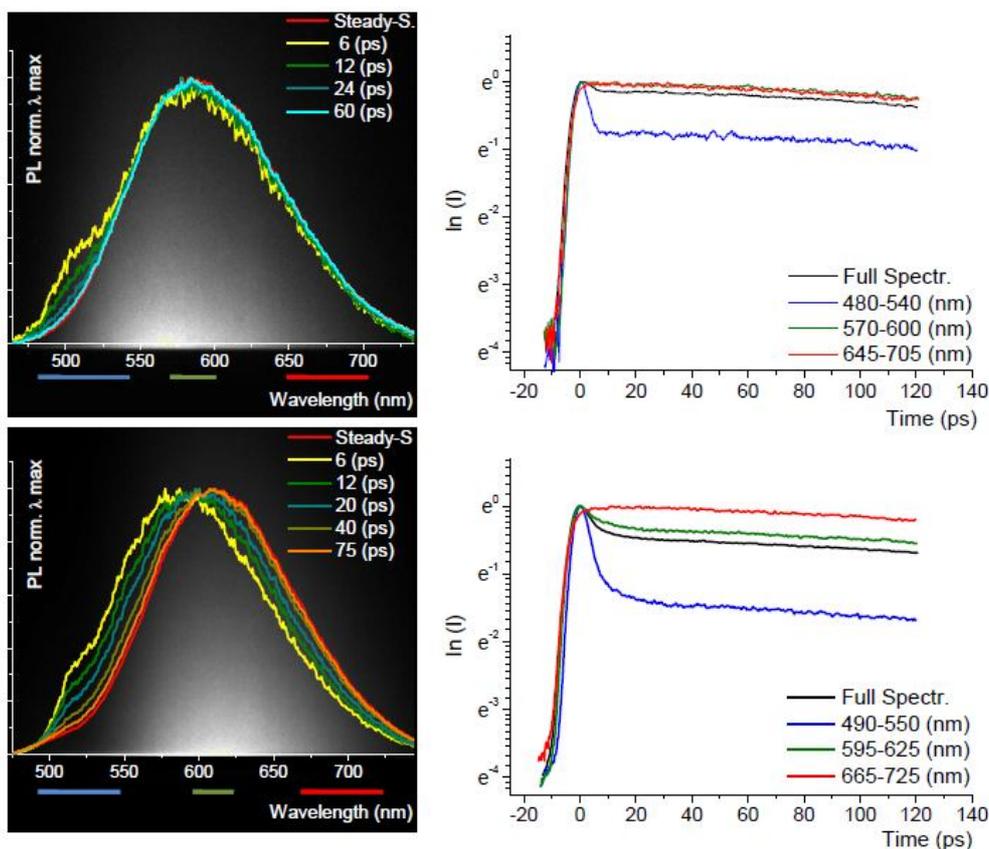
Figure 3.8 *Transient PL spectra at different times and normalized PL decays at different emission wavelength measured for T4DIM in acetonitrile and dimethylsulfoxide respectively. Excitation with a laser pulse at 442 nm. The time-resolved fluorescence intensities were fitted with a two-exponential function.*

Solvent	Range (nm)	Time (ps)	
CH$_3$CN	Full Spectr.	τ: 585	
	480-540	τ_1: 6.0; A$_1$: 0.35	τ_2: 685; A$_2$: 0.65
	570-600	τ: 595	
	645-705	τ: 543	
DMSO	Full Spectr.	τ_1: 8.5; A$_1$: 0.23	τ_2: 676; A$_2$: 0.87
	590-550	τ_1: 8.0; A$_1$: 0.60	τ_2: 676; A$_2$: 0.40
	595-625	τ_1: 9.2; A$_1$: 0.12	τ_2: 774; A$_2$:0.88
	665-725	τ_1: 714	

Table 3.4 *Time components (τi) and preexponential factors (Ai) obtained from the fitting of fluorescence time decays of T4DIM solutions in acetonitrile and dimethylsulfoxide.*

3.3 Theoretical Analysis

In order to support and rationalize our experimental data, the influence of the polar environment on the excited state properties was investigated theoretically with density-funtional theory (DFT) calculations. Analysis of the electronic structures of the molecule was carried out both in vacuum and in *CH₃CN* solution. The TDDFT calculations of the lowest singlet–singlet excitations were performed using MPW1K functional and 6-31g* basis set. The frontier molecular orbital (MO) contribution is very important in determining the charge-separated states of the model oligomers. In fact, to create an efficient charge-separated state, the highest occupied MO (HOMO) must be localized on the extended donor moiety and the lowest unoccupied MO (LUMO) on the acceptor moiety. The isodensity plots of the **T4DIM** are shown in *Figure 3.11*. The HOMO state density is distributed entirely over the conjugated thiophene units, while the electron density of the LUMO level is extended on the acceptors moiety, that is strongly influenced by quinoidal/cumulenic configurations.

It is interesting to note that a significant contribution to the LUMO comes from the electron-accepting diimide groups. As shown before, the comparison between the absorption spectra of T4DIM and DH4T revealed a decrease of the optical energy band gap by the introduction of the diimide segment. In *Figure 3.12* are reported the HOMO and LUMO energy levels for both DH4T and T4DIM molecules in vacuum.
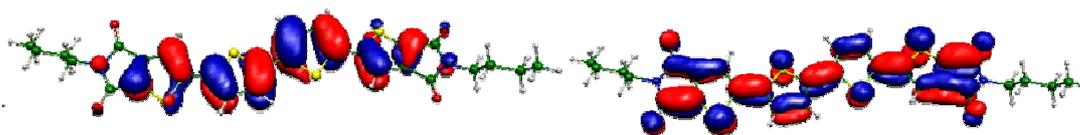
Figure 3.11 *Isodensity plots (isodensity value = 0.035) of the HOMOs (left) and LUMOs (right) of T4DIM.*
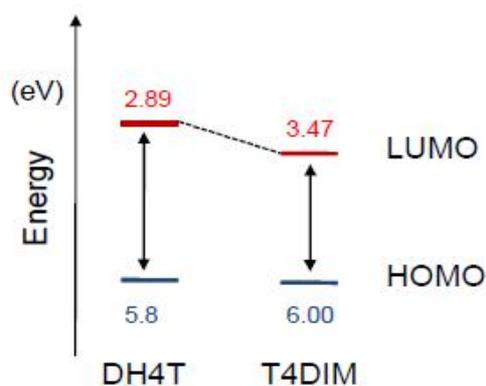
The main geometrical parameters of the investigated molecular system in the ground and in the lowest excited states are collected in *Table 3.6*. Comparing the ground- and excited-state optimized geometries of **T4DIM** we found significant differences (*Figure 3.13*). In polar solvent environment such as acetonitrile, the computed dihedral angles, which a parameter of the planarity of the molecules are strictly different in ground and excited states[98]. Indeed in the excited state the molecule is planar while in the ground state the thiophene units is distorted. In the excited state we also observe a reduction of the C-C length in the thiophene units *Table 3.6*. These results are in good agreement with the PICT model given that the electronic coupling between the donor and the acceptor groups in ICT state planarizes the donor and acceptor systems, which results in a large dipole moment.
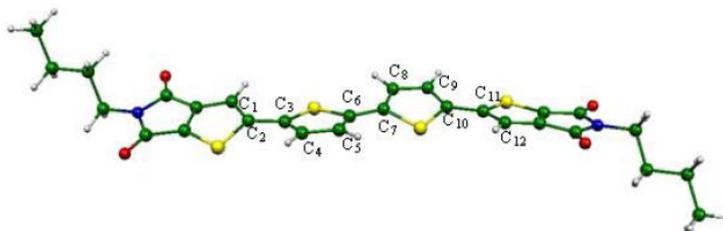
***Figure 3.13** Optimized molecular structure of **T4DIM** in the ground state.*

Length(Å)	S0	S1
C_2-C_3	1.45	1.40
C_6-C_7	1.45	1.39
C_{10}-C_{11}	1.45	1.40

Angle(°)	S0	S1
<C_1-C_2-C_3-C_4	160.7	-179.9
<C_5-C_6-C_7-C_8	-162.5	180
<C_9-C_{10}-C_{11}-C_{12}	160.9	179.9

***Table 3.6** Comparison between optimized geometrical parameters (Å and °) of T4DIM molecule in ground and excited state in CH₃CN.*

It should be noted that the PICT model proposed in this system is different from the PICT in which it is assumed that a sufficiently small energy gap between the two interacting states S_1 and S_2 leads to a solvent polarity induced pseudo-Jahn–Teller coupling. The PICT model used in this thesis is based on the second assumption that each dihedral angle are stable planar structure induced by the polar solvent. As the electronic coupling between the donor and the acceptor subsystems increases, the degree of conjugation of the compound also increases, and subsequently promotes the charge and energy transfer from the thiophene core to the diimide subsystem

(promotes the EL state switches to the ICT state), and results in the increases of the transition dipole moment.

References

[74] (a) Weitz, R. T.; Amsharov, K.; Zschieschang, U.; Villas, E. B.; Goswami, D. K.; Burghard, M.; Dosch, H.; Jansen, M.; Kern, K.; Klauk, H. *J. Am. Chem. Soc.* **2008**, 130, 4637. (b) Ling, M.-M.; Erk, P.; Gomez, M.; Koenemann, M.; Locklin, J.; Bao, Z. *Adv. Mater.* **2007**, 19, 1123.

[75] Gao, X.; Wang, Y.; Yang, X.; Liu, Y.; Qiu, W.; Wu, W.; Zhang, H.; Qi, T.; Liu, Y.; Lu, K.; Du, C.; Shuai, Z.; Yu, G.; Zhu, D. *Adv. Mater.* **2007**, 19, 3037.

[76] For a recent review, see: Sakai, N.; Mareda, J.; Vautheyb, E.; Matile, S. *Chem. Commun.* **2010**, 46, 4225.

[77] (a) Wang, Z.; Kim, C.; Facchetti, A.; Marks, T. *J. Am. Chem. Soc.* **2007**, 128, 13362. (b) Li, Y.; Tan, L.; Wang, Z.; Qian, H.; Shi, Y.; Hu, W. *Org. Lett.* **2008**, 10, 529. (c) Yan, H.; Chen, Z.; Zheng, Y.; Newman, C.; Quinn, J. R.; Dotz, F.; Kastler, M.; Facchetti, A. *Nature* **2009**, 457, 679.

[78] Mishra, A.; Ma, C.; Bäuerle, P. *Chem. Rev.* **2009**, 109, 1141.

[79] (a) Yamada, K.; Okamoto, T.; Kudoh, K.; Wakamiya, A.; Yamaguchi, S.; Takeya, *J. Appl. Phys. Lett.* **2007**, 90, 072102. (1) ; (b) Xiao, K.; Liu, Y.; Qi, T.; Zhang, W.; Wang, F.; Gao, J.; Qiu, W.; Ma, Y.; Cui, G.; Chen, S.; Zhan, X.; Yu, G.; Qin, J.; Hu, W.; Zhu, D. *J. Am. Chem. Soc.* **2005**, 127, 13281. (c) Li, X.-C.; Sirringhaus, H.; Garnier, F.; Holmes, A. B.; Moratti, S. C.; Feeder, N.; Clegg, W.; Teat, S. J.; Friend, R. H. *J. Am. Chem. Soc.* **1998**, 120, 2206.

[80] (a) Zou,Y.;Najari,A.;Berrouard,P.;Beaupre, S.;Ach,B.R.;Tao, Y.; Leclerc, M. *J. Am. Chem. Soc.* **2010**, 132, 5330. (b) Piliego, C.; Holcombe, T. W.;Douglas, J.D.; Woo, C. H.; Beaujuge, P.M.; Frechet, J. M. J. *J. Am. Chem. Soc.* **2010**, 132, 7595. (c) Zhang, Y.; Hau, S. K.; Yip, H.-L.; Sun, Y.; Acton, O.; Jen, A. K.-Y. *Chem.Mater.* **2010**, 22, 2696. (d)Zhang, G.; Fu, Y.; Zhang, Q.; Xie, Z. *Chem. Commun.* **2010**, 46, 4997.

[81] (a) Letizia, J. A.; Salata, M. R.; Tribout, C. M.; Facchetti, A.; Ratner, M. A.; Marks, T. J. *J. Am. Chem. Soc.* **2008**, 130, 9679. (b) X. Guo, R. P. Ortiz, Y. Zheng, Y. Hu, Y.-Y. Noh, K.-J. Baeg, A. Facchetti and T. J. Marks, *J. Am. Chem. Soc.*, **2011**, 133, 1405.

[82] Wei Hong, Haihong Yuan, Hongxiang Li, Xiaodi Yang, Xike Gao and Daoben Zhu. *Org. Lett.*, Vol. 13, No. 6, **2011**

[83] Manuela Melucci, et al.*Chem. Commun.*, **2011**, **47**, 11840–11842

[84] (a) X.S. Xie, J.K. Trautman, *Ann. Rev. Phys. Chem.* 49 (**1998**) 441. (b) E.J.G. B. Nielsen and T. Bjørnholm, *Org. Lett.*, **2004**, **19**, 3381.

[85] C. O. Kappe, *Chem. Soc. Rev.*, **2008**, 37, 1127.

[86] M. Melucci, G. Barbarella, M. Zambianchi, P. Di Pietro and A. Bongini, *J. Org. Chem.*, **2004**, 69, 4821.

[87] A. Facchetti, M.-H. Yoon, C. L. Stern, G. R. Hutchison, M. A. Ratner and T. J. Marks, J. Am. Chem. Soc., 2004, 126, 13480;

[88] Hiroshi Yao, Kaori Domoto, Takeshi Isohashi and Keisaku Kimura, *Languir* **2005**, 21, 1067-1073

[89] Joseph R. Lakowicz, *Principles of Fluorescence Spectroscopy* Springer Edition

[90] E. Lippert, W. Ltlder, F. Moll, H. Nagele, H. Boos, H. Prigge, 1. Siebold-Blankenstein, *Angew. Chem.* 73 (**1961**) 695.

[91] (a) K. Rotkiewicz, K.H. Grellmann, Z.R. Grabowski. *Chem. Phys. Lett.* 21 (**1973**) 212; (b) A. Siemiarczuk, Z.R. Grabowski, A. Krowczyriski, M. Asher. M. Gttolenghi. *Chem. Phys. Lett.* 5 1 (**1977**) 3 15; (c) Z.R. Grabowski, K. Rotkiewicz, W. Rettig, *Chem. Rev.* 103 (**2003**) 3899; (d) A. Ko¨hn, C. Ha¨ttig, *J. Am. Chem. Soc.* 126 (**2004**) 7399.

[96] (a)Th. von der Haar, A. Hebecker, Yu. Il'ichev, Y.-B. Jiang, W. Ktlhnle, K.A. Zacharlasse, *Rec. Trav. Chim. Pays-Bas* 114 (**1995**) 430; (b) K.A. Zacharlasse, M. Grobys, Th. von der Haar, A. Hehecker, Yu.V. Il'ichev, Y.-B. Jiang, O. Morawski. W. Kiihnle, *J. Photochem. Photobiol A: Chem.* 102 (**1996**) 59; (c) S. Techert, K.A. Zachariasse, *J. Am. Chem. Soc.* 126 (**2004**) 5593.

[98] Mengtao Sun, *Chemical Physics Letters* 408 (**2005**) 128–13

Chapter 4

Photophysical properties of T4DIM ultra thin-films

In this chapter we report on a comprehensive investigation on the correlation between the photo-physical properties and the morphological arrangement of T4DIM semiconductor thin-films at the early stage of growth onto substrates widely used in OLETs. This study is held by cross-correlating detailed time-resolved and energy-dispersed photoluminescence spectroscopy at low temperature together with microscopic scanning probing tools such as confocal laser scanning microscopy (CLSM) and atomic force microscopy (AFM). The optoelectronic characteristics of the OLETs fabricated implementing T4DIM as at different growth conditions are also reported.

4.1 Introduction: Role of molecular packing in determining solid-state optical properties of π-conjugated materials.

The optical and electronic properties of π-conjugated materials in devices, which essentially deal with solid films, are defined not only by the chemical structure of the constituent molecules but also by the nature of their intermolecular electronic coupling. The nature of intermolecular interactions in solid films is, in turn, defined by the relative orientation of the nearest-neighbor molecules. In planar π-conjugated materials increased, overlap between π-orbitals of neighboring molecules results in delocalization of the polarons/excitons, leading to reduction in the activation barrier for charge transport, thereby increasing charge carrier mobilities, with the hopping mechanism playing a major role[99,100]. Such interactions, on the other hand, open new pathways for the nonradiative decay of excitons which can compete with emissive routes, resulting in the quenching of solid-state luminescence, a phenomenon commonly referred to as concentration quenching[101,102]. Thus, the two major issues that need to be addressed for the design of active elements in

organoelectronic devices, namely, efficient charge transport and strong luminescence, are oppositely related. For tuning properties of materials in devices, it is therefore necessary to have a detailed understanding of the dependence of the charge transport and luminescence properties on the relative positions of adjacent molecules as well as on the factors that determine the nature of molecular packing in the solid state. Information on the dependence of solid-state optical properties on molecular packing can reliably be obtained from X-ray and photophysical analysis of single crystals.

4.2 X-ray analysis of T4DIM in single crystal and thin film.

The X-ray intensity data for **T4DIM** were measured on a Bruker SMART Apex II CCD area detector diffractometer. Cell dimensions and the orientation matrix were initially determined from a least-squares refinement on reflections measured in three sets of 20 exposures, collected in three different ω regions, and eventually refined against all data. For all crystals, a full sphere of reciprocal space was scanned by 0.3° ω steps. The software SMART was used for collecting frames of data, indexing reflections and determination of lattice parameters. The collected frames were then processed for integration by the SAINT program, and an empirical absorption correction was applied using SADABS. The structures were solved by direct methods (SIR 97) and subsequent Fourier syntheses and refined by full-matrix least-squares on F^2 (SHELXTL), using anisotropic thermal parameters for all non-hydrogen atoms. The hydrogen atoms bound to carbons were located in the Fourier maps, added in calculated positions, included in the final stage of refinement with isotropic thermal parameters, $U(H) = 1.2\ U_{eq}(C)$ [$U(H) = 1.5\ U_{eq}(C\text{-Me})$], and allowed to ride on their carrier atoms. Crystal data and details for the data collection for **1** are reported in *Table 4.1*.

Crystal symmetry	Triclinic
Space group	*P-1*
a, Å	4.841(4)
b, Å	11.278(7)
c, Å	12.907(9)
α, °	71.880(9)
β, °	86.80(1)
γ, °	86.93(1)

Table 4.1 *Cell Parameters*

Single Crystal XRD

The X-ray crystal structure of T4DIM is shown in *Figure 4.1*. The molecule lies on a crystallographic inversion center located at the midpoint of the bond between the two thiophene units. The molecular backbone is almost planar being the two inner thiophene rings strictly coplanar and the dihedral angle between the thiophene and the thiophene-imide units $4.4(5)°$. The crystal packing (*Figure 4.1a*) shows that the molecules adopt a slipped π–π stacking packing mode (interplanar distance ca. 3.51Å, sliding along the long molecular axis 3.32Å) instead of the herringbone structure more common for oligothiophenes[103] including the recently reported *dithieno-[2,3-b:3'2'-d]thiophene diimide*[104]. The molecules of adjacent π–π stacks are engaged in supramolecular 1D networks running across the *bc* plane formed through two intermolecular C–H···O H bonds ($H_{11}B$···O_1 2.54 Å (one for each fused ring) C_{11}···O_1 3.48(1) Å, C_{11}–$H_{11}B$···O_1 162°, *Figure4.1b*) in which two oxygens in anti position interact with one hydrogen of the carbon directly attached to the nitrogen of the imide unit of two different molecules.
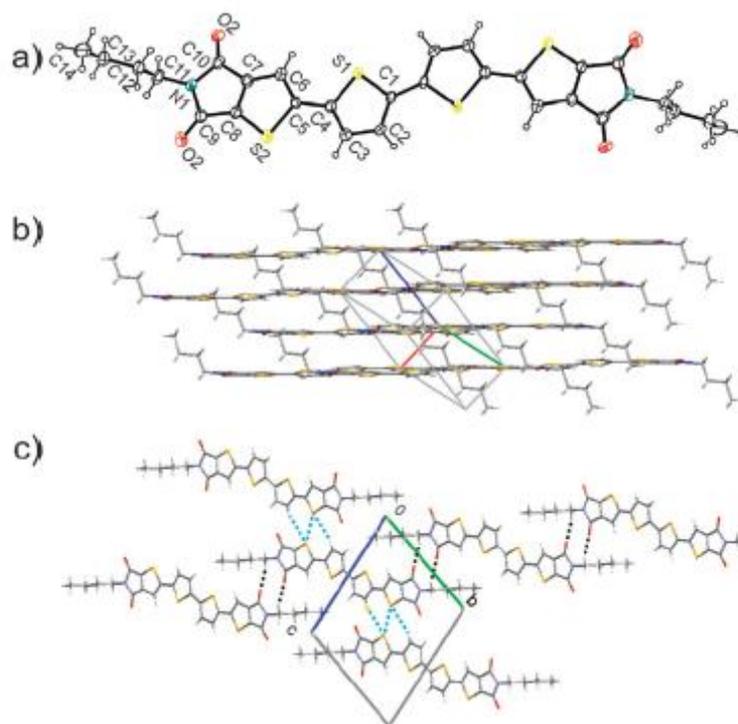
Figure 4.1 *(a) ORTEP drawing of T4DIM (displacement ellipsoids drawn at the 30% probability level). Unlabeled atoms are related to the labeled atoms by the symmetry operation: 2 -x, -y, 1-z. (b) Arbitrary view of the crystal packing showing the π–π stacks.(c) View along the axis of one 1D network generated by C–H•••O interactions (dashed black). S•••S and C–H•••S contacts (light blue).*

Moreover, intermolecular contacts involving the sulfur atoms of the fused imidothiophene rings (S···S contacts 3.73 Å , sum of the sulfur van der Waals radii 3.7 Å)[105] of neighbor molecules not participating in the C–H···O interactions were found. The same sulfur atoms are also engaged in weak C–H···S interactions (C–H···S, H···S 3.03 Å) with the inner hydrogens of the thiophene rings.

Thin Film and powder XRD

The XRD patterns of the powder sample together with those of cast, cast-melt-quenched and vacuum sublimed films are displayed in *Figure 4.2*. They show several well resolved diffraction peaks confirming an important degree of crystallinity. The most intense peaks correspond to the first and second order of a periodicity of 2.46 nm. Both peaks are present either in powder or in film samples. The cast film profile shows overall the same reflections of the powder sample, suggesting the same phase and a random orientation of the crystal domains in the film. After melting at 285 °C and rapid cooling at RT, only the two peaks in the small angle region are appreciable, but at high magnification other reflections, due to higher order periodicity of the 2.46 nm distance (up to the 10th) are found. Being the molecular length about 2.8 nm and the projection on its main plane 2.6 nm, the period measured from the XRD pattern of film samples, suggests an almost perpendicular arrangement of the molecules respect to the substrate (*Figure 4.2e*).
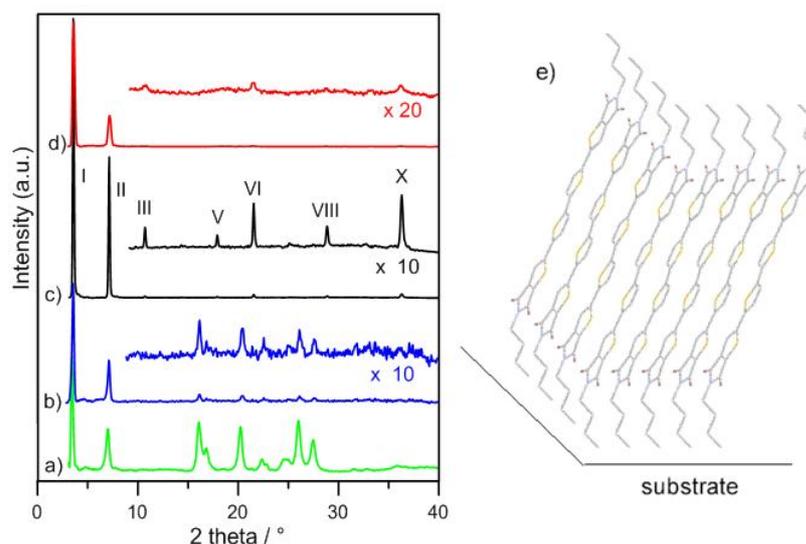
Figure 4.2 XRD patterns of a) the powder; b) cast film; c) cast-melt-quenched film; d) film of T4DIM sublimed in vacuum on SiO$_2$ substrate (thickness 20 nm); e) sketch of the molecular arrangement in film samples. In roman numerals the order of the 2.46 nm periodicity.

4.3 Thin-films of T4DIM on different substrates

4.3.1 Introduction

As show in precedent section, the crystal packing of molecular organic materials results from a large complex balance of several intramolecular interaction within a narrow energy range of less than 1 *eV,* including hydrogen bond, π overlap, elettrostatic and Van der Waals force. In addition to the interaction within the crystal, interactions at the interface should be taken into account in the case of thin-film formation. Because these interactions are in general weak, highly crystalline structures can be formed without the necessity of lattice matching. Different crystallographic phases, type and degree of orientation and surface morphologies can be achieved, depending on the chemical nature of the surface energy and the chosen kinetic of growth[106]. For instance in submonolayer films of *sexithiophene* (T6), a coexistence of two phases composed, by molecules perpendicular and parallel to the substrate, it has been demonstrated by CLSM and spatially resolved spectroscopy[107] *(Figure 4.3)*. The presence of flat lying molecules on SiO$_2$ depends on the variable density of OH group on the substrate surface.
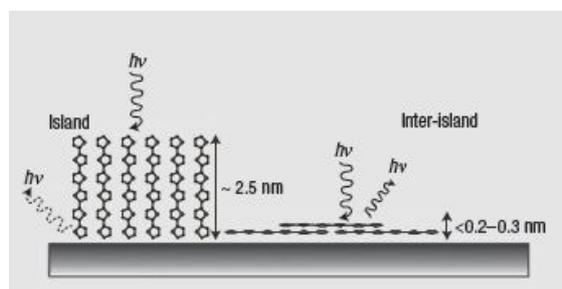
Figure 4.3 *Sexithiophene (T6) in the early stage of growth*

When the first monolayer is completed, all T6 molecules stand on the substrate, and the flat molecules detected in the submonolayer films are no longer present. In films that are thicker than two monolayers, the photoluminescence spectra of standing molecules show a molecular H-like aggregation as in the single crystal. To better understand, the influence of different substrates on the molecular packing of **T4DIM**, I studied thin-films of this material deposited on quartz and two different polymer

dielectrics, compatible with all-plastic OFETs: PMMA (*polymethylmetaacrylate*) and PVK (*polyvinylcarbazole*) respectively (*Figure 4.4*).
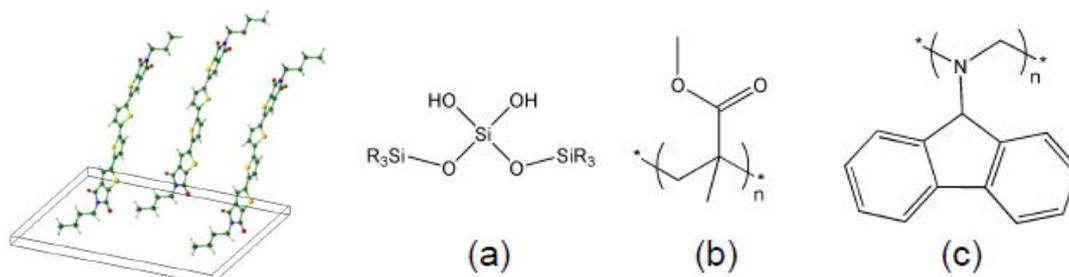
Figure4.4 *Thin- Folms of T4DIM on different substrates a) Quarz b) PMMA, c) PVK. Contanct Angles 48°, 69°, 83° rispectivaly.*

All samples has been made at the same rate of growth (0.01 A/s) with a nominal thickness of 2 *nm*. The differences between the surfaces has been qualitatively estimated by measuring the contact angle using water as solvent

4.3.2 Steady-state absorption and fluorescence

When **T4DIM** is deposited onto different substrates by vacuum sublimation, the resulting spectral shape of the solid-state spectra is quite different, from that observed in acetonitrile solution, as it can be seen in *Figure4.5a*. In all thin film samples, a long tail extending past 480 *nm* and blue shift of the main absorption peaks at 450-375 *nm* are observed.
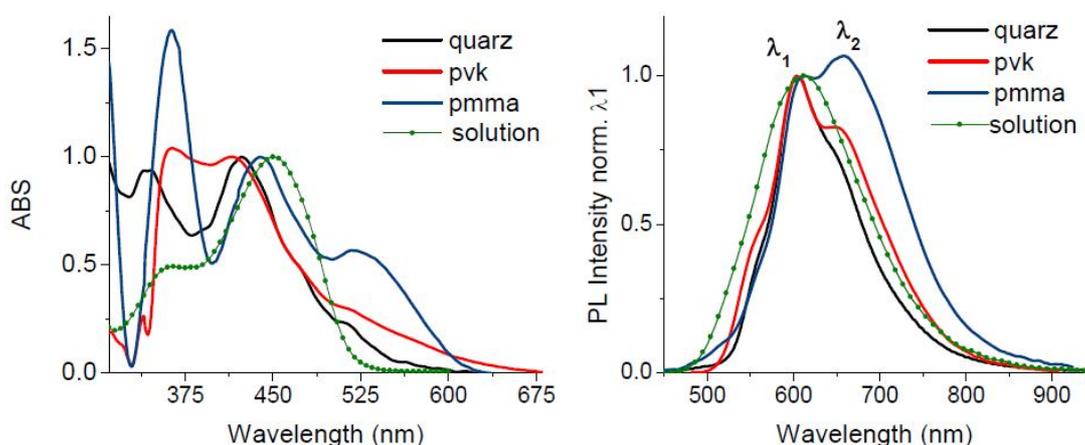
Figure 4.5 *Comparison of the absorption **a)** and emission spectra (wavelength excitation 442nm) **b)** at room temperature of T4DIM in thin films (nominal thickness 2nm) on quarz (black line) , PMMA (polymethylmetacrylate) (red line), PVK (polyvinylcarbazole) (blue line) and acetonitrile solution 10^{-6}M (red line).*

In particular, the intensity of the absorption band at lower energy increases as the nature of the surface changes passing from quartz, PVK to PMMA with a progressive red shift. The steady – state PL spectra for all thin film samples exhibits two characteristic luminescence peaks λ_1, λ_2 and a band as a shoulder at 550 *nm* (*Figure 4.5b*). The comparison of the emission profiles between acetonitrile solution and thin films also in this case shows substantial differences. In fact, the position of the maximum emission in solution does not change so much respect to the peak position λ_1 for all thin film samples. While, a significant red shift for the peak λ_2 it has been observed together with an increase of its relative contribution into the overall PL spectra; specially for PMMA sample. This behavior in steady-state spectra is also dependent on the excitation wavelength. Indeed, exciting all T4DIM films at high energy (375 *nm*) the relative intensity of λ_2 is higher than that observed at low excitation wavelength (442 *nm*).

Although the fluorescence spectra in thin films are structured with respect to the solution it is interesting to note that both emission are in the same spectral region. This result can be due to the planarization of the T4DIM molecules configuration in both cases. In fact, as shown in last section the emission of T4DIM in solution is strongly influenced by the solvent polarity, in particular in solvent such as acetonitrile the emission is dominated by ICT state in which the molecules is assumed to be planar. The same configuration is found also for T4DIM in solid state in which the planarity is promoted by the presence of multiple hydrogen-bonds between neighbor T4DIM molecules (*Figure 4.1c*).

Discussion

The differences in absorption spectra, between the solution (when the molecular overlap between nearest neighbor molecules is insignificant) and the thin films (characterized by a collective response of the molecules) reveal that the spectral changes in solid state can be due to specific intermolecular interactions between the molecules. For instance, a *blue shift* of the maximum absorption in solid state is common referred to H-aggregates in which the molecules are orientated one on top of the other to form a strong π overlap. This interaction decreases by a displacement along the molecular axis of the molecules. It causes a head to tail arrangement characteristic of J-dimer and a *red shift* of the absorption peaks are observed. From the spectral features of T4DIM in thin-films both J- and H- bands seem to be present

and their relative contribution depends on the nature of the substrate surface. Although for π-conjugated oligomers a few observation of J aggregation with the concomitant presence of other species such as H-aggregation and excimers have been reported[108] it remains to be demonstrate how these aggregates can be obtained in thin films. Two main factors must be to considered. organic semiconductors are characterized by a relatively low symmetry of the growth units, and this originates a huge variety of defect configurations which are reminiscent of the mechanisms of aggregation of molecules.

moreover, the weak cohesive intermolecular interaction between the molecules enables a different crystallographic ordering (*polymorphism*). Most of the different technique used for the preparation of thin film are not only capable of producing large areas of known crystallographic phases, but also a new phases. In addiction they first allow the stabilization of some of them which are metastable. At instance for *hexaphenyl*, the β phase is obtained by physical vacuum deposition when the substrate are held at room temperature, while a new phase(γ) is obtained when the substrates are heated to 160°C[109]. The XRD analysis on T4DIM film, after heat-treating and rapid cooling, proves that for this compound is possible to consider a different molecular packing of T4DIM molecules with respect the well-know crystal structure (*Figure 4.2c*). Despite the experimental findings, the detailed structure of the different new polymorphic phase still remains to define. In any case the spectral features in both the absorption and fluorescence spectra can be rationalized in terms of coexisting polymorphic aggregates in thin films.

4.3.3 PL at low temperature

The steady state photoluminescence spectra at low temperature are shown in *Figure 4.6*. The temperature dependence of the fluorescence spectra is clearly different in all samples. As the temperature decrease, two factors contributes to the spectral changes: the relative intensity of the band peaked at λ_1 and λ_2 , a different shift of the λ_2 component.
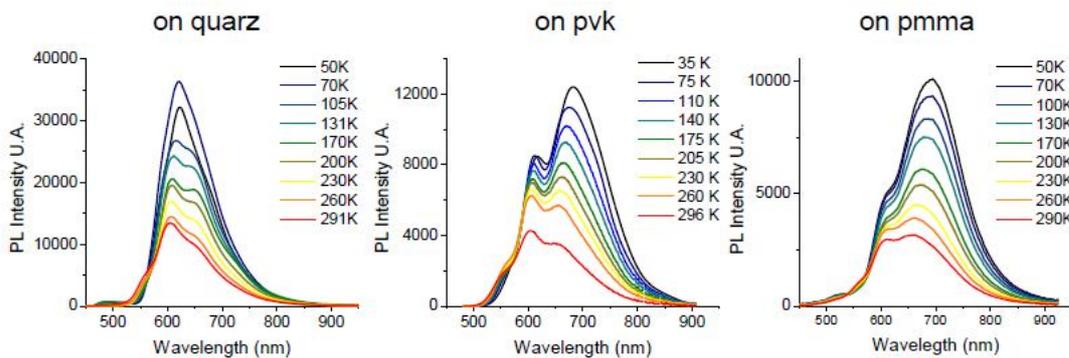
Figure 4.6 *Steady-state fluorescence at low temperature of T4DIM thin films (2nm) on different substrates: a) quarz, b)PMMA, c) PVK (wavelength exc. 375 nm).*

In the case of T4DIM on quarz, the emission spectrum at 50 *K* is characterized by a single emission band centered at 620 *nm* with a full width at half maximum (FWHM) that is reduced with respect to the band at 291 *K*. On the other hand, in PVK and PMMA samples, the two emission components can be recognized also at lower temperature. In particular, in both PVK and PMMA substrates the fluorescence spectra of T4DIM shows the same red shift for λ_2 peak (35 *nm*) in going from room temperature to 50 *K*. Here, the main difference concerns the relative intensity of the two components. At instance, as the temperature decreases the intensity of the band peaked at λ_2 of T4DIM on PMMA substrate is higher than PVK substrate.

Discussion

A blue shift of the steady state PL spectrum with increasing temperature has been previously observed in thermally evaporated molecules and in conjugated polymers[110-111]. Due to disorder in these materials the density of excitonic states (DOS) is not homogeneously broadened (*see Figure 4.7*).
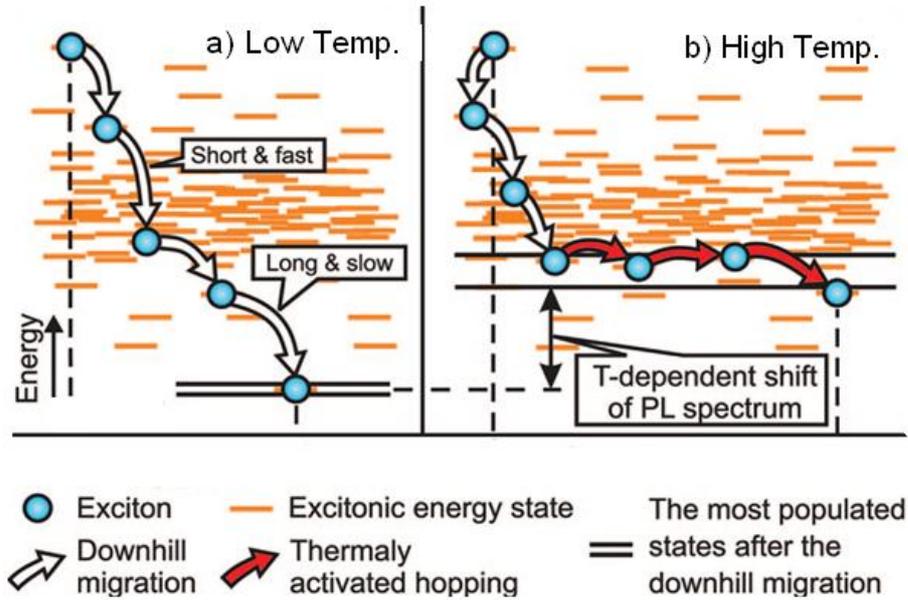
Figure 4.7 *The Gaussian density of states is represented by the distribution of the energies of excitonic states. The T-dependent shift of the PL spectrum maximum is originated by the exciton-phonon coupling, which determines the position of the energy level of the most populated states.*

The creation of excitons in the high energy tail of the DOS by absorption of UV light is followed by their downhill migration toward lower energy sites. Then the relaxation ends when excitons reach the energy level of the most populated states.

At low temperatures (*Figure 4.7a*), such a level is situated deep in the tail of the Gaussian DOS, whereas at high temperatures excitons are thermally distributed closer to the middle of the DOS (*Figure 4.7b*). The energy increase of the level of the most populated states with temperature causes the blue shift of the PL spectrum.

In agreement with this model, the downhill migration in T4DIM thin films brings excitons to the level of the most populated states. Further hopping requires absorption/emission of a phonon, consequently the sample temperature starts to play a role. At low temperatures the exciton-phonon coupling is weak and excitons cannot hop any more. Thus, in this case, the migrations of the exciton is limited by the *downhill migration process* that determine a red shift in emission spectra specially for the λ_2 component. As temperature increases, the probability of phonon absorption by excitons increases. The level of the most populated energy sites climbs uphill on the DOS leading to the decrease of the energy difference between the occupied and neighboring sites. If the temperature is high enough, the *thermally activated hopping* becomes favorable as a consequence the intensity of λ_1 component increases. It does not lead to a significant change of the exciton energy but contributes to the exciton diffusion. The spectral changes at low temperatures of T4DIM thin films are a

clearly indication about the relative disorder of that molecules when sublimated onto different substrates.

4.3.4 AFM and CLSM investigation

In order to find other correlation about the systematic differences observed in absorption and fluorescence spectra between T4DIM films depositated on quarz, PVK and PMMA, I studied also the morphology of each films by AFM in tapping conctact mode *Figure 4.8* and by CLSM *Figure4.9*.
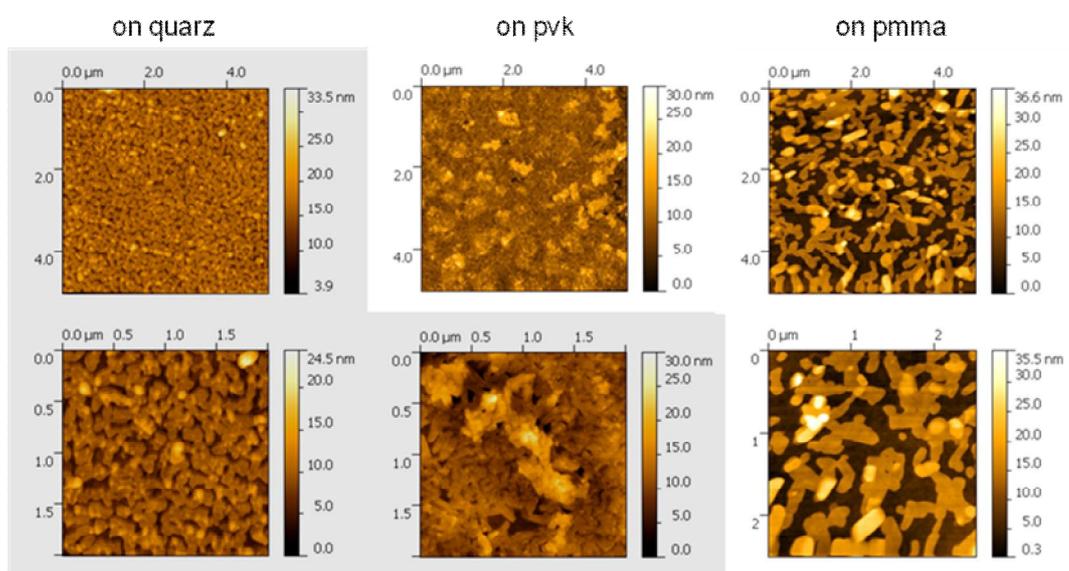
Figure4.8 *Morphological investigation by Atomic Force Microscopy (in tapping mode) of T4DIM thin films.*

In the early stage of growth, the island height is larger than the nominal film thickness, in all substrates. This indicate that the T4DIM films grow in a three dimensional mode (*Volmer-Weber* like growth[112]) in accord to the perpendicular arrangement found in the XRD analysis. The size and the coalescence of the island depend on the nature of the substrate. In particular as revealed by AFM images, the morphology of T4DIM on quarz, is characterized by small microcrystals with high density, so that full substrate coverage is already achieved at 2 *nm* nominal thickness. From the evolution of the height and shape of the islands it is clear the coexistence of different topologies, in particular for T4DIM grown on PVK and PMMA substrate. These results are also confirmed by CLSM (*see Figure 4.9*). In both samples, the aggregates range in size from a few hundred nanometers in diameter to over a micron.
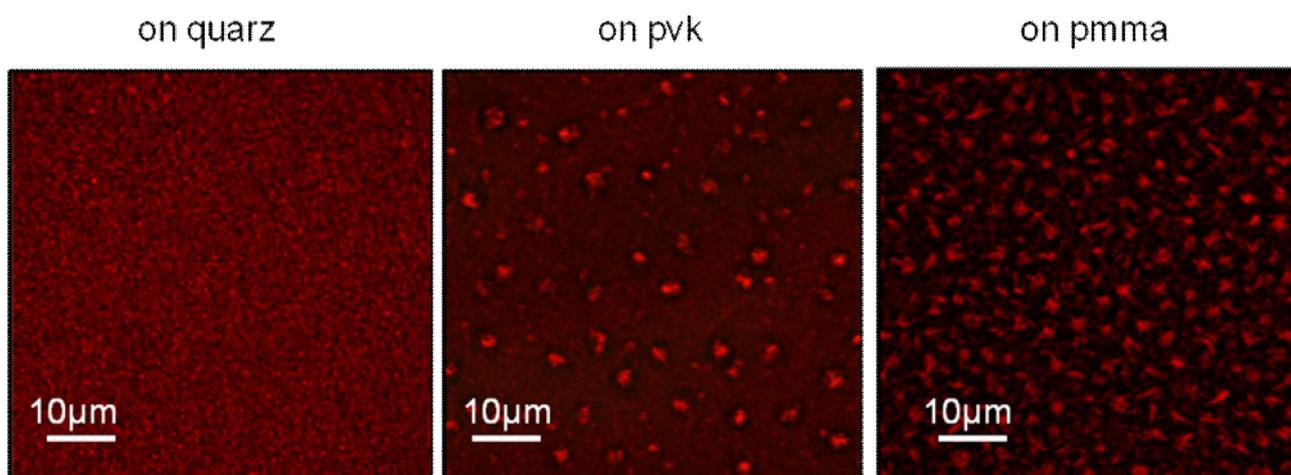
Figure 4.9 *Morphological investigation by CLSM of T4DIM thin films (wavelength excitation 488 nm, objective:100 x oil, pinhole: L, red channel 8.20).*

4.3 T4DIM on PMMA substrate

In the precedent section we showed the influence of different surfaces on the molecular organization in the early stage of growth of T4DIM. The spectral features in absorption and in emission depend on how the molecules pack in the solid into aggregates. In particular, it has been proposed, the occurrence of aggregates in terms of coexisting polymorphs in thin films.

Now, I want to focus the interplay between the kinetics of growth and the self organization of the T4DIM molecules when they are sublimated on PMMA substrate. The kinetics of the film growth by high vacuum sublimation is governed by parameters such as deposition rate, temperature of the substrate, and amount of deposited material (i.e., time of deposition or film thickness). In order to investigate the properties of T4DIM molecules under different regime of growth, I studied, by atomic force microscopy (AFM), photoluminescence spectroscopy at low temperature and resolved in time, a set of different films in which T4DIM have grown on PMMA/ITO/glass substrate. All T4DIM films are stable over time. Using two deposition rate 0.1 and 0.01 *Å/s* it is generated a set of three samples with different thickness 2, 5 and 10 *nm* for each of the mentioned deposition rate.

A sequence of AFM images for all samples is represented in *Figure4.10*. The actual growth behavior can be different if growth kinetics dominates over the self-organization of the T4DIM molecules. In fact, T4DIM shows different morphologies on PMMA surface (where it is assumed the same adhesion energy between the dielectric layer and T4DIM) for different deposition rates.
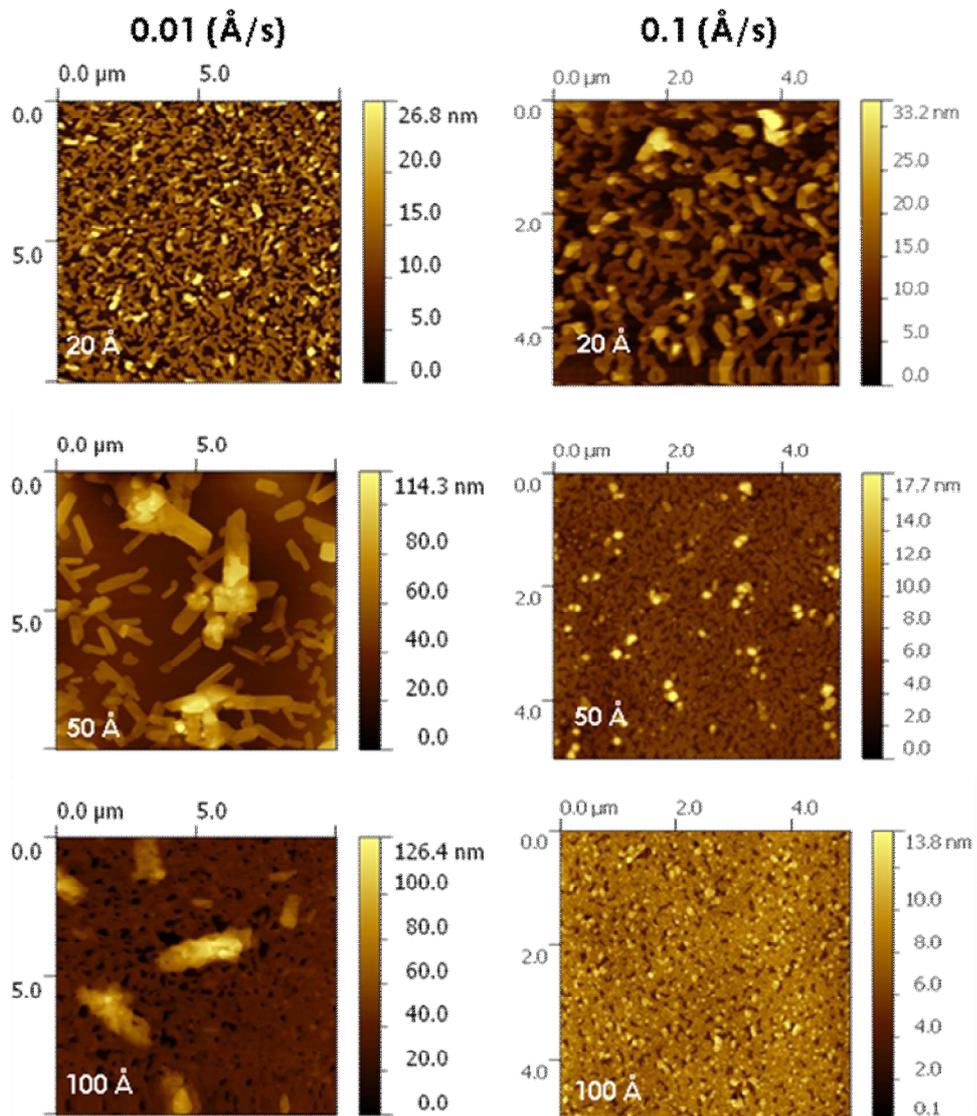
Figure 4.10 *AFM images of T4DIM samples grown on pmma substrate. Topological strusctures obtained at different deposition rate, [0.01 and 0.1(Å/s)] and film thickeness increasing from 2 to 10 nm*

This result proves that the growth behavior of T4DIM thin films is dependent not only by the adhesion energy as shown in the last section. At the early stages, corresponding to one-two monolayer, T4DIM grows with nucleation of three-dimensional aggregates that coexist with two-dimensional islands. For the higher sublimation rate (*0.1Å/s*), there are large islands and low island density. As the thickness layer increases a full substrate coverage is achieved at 5 *nm* and the coexistence of different topologies is still clear. Then a 10 *nm* of nominal thickness the morphology changes only slightly with a decrease of the average roughness (*Figure 4.11*). Whereas for the lower kinetics of growth (*0.01Å/s*) an increase of the nucleation aggregates in sample thicker 2 *nm* is observed. Then, the evolution of the

morphology versus the film thickness clearly shows that a morphological transition occurs between 2 and 5 *nm* of nominal thickness and full substrate coverage is achieved only at 10 *nm.*

PL at low temperature

In *Figure 4.12* the steady-state PL spectra at low temperature for all samples are shown, whose morphology can be ascribed to the typical molecular architectures evidenced in *Figure 4.10*. For T4DIM grown onto PMMA substrate the temperature dependence of the emission spectra has been studied only for the sample with 2 *nm* of nominal thickness. As the temperature decreased a bathochromical shift of the low energy component together with an increase of its relative intensity has been found. These spectral features at low temperatures become less evident when the thickness of the deposited material increases. As the film morphology changes from films thicker 2nm to films of 10 *nm* of nominal thickness, the difference in emission spectra is mainly determined by the decrease of the number of aggregates states with the number of the layers.
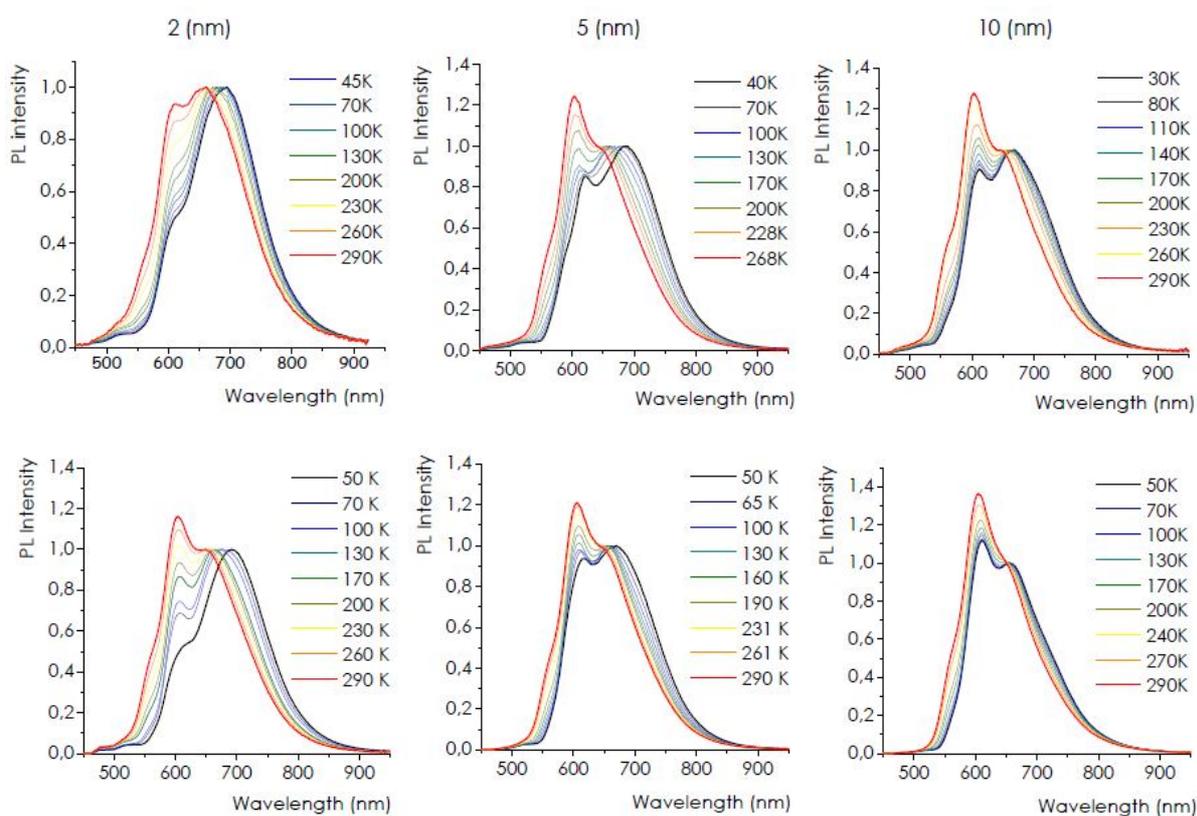
Figure 4.12 *Photoluminescence spectra at low temperature for T4DIM thin films grown onto PMMA at different thickness (from left to right 2, 5 and 10 nm) and different deposition rate (0.01Å/s up, 0.1Å/s down). Wavelength excitation 375 nm.*

These behavior nevertheless is dependent by the kinetics of growth. In fact, as shown in the AFM images, at low deposition rate a morphological transition between the sample of 2 and 5 *nm* has been observed. The corresponding PL spectrum shows that the characteristic red shift of λ_2 at low temperature is still more pronounced while it is reduced at higher deposition rate.

These results are in agreement with the hypothesis that an aggregates emission from low energy states contributes into the overall PL spectra. This emission becomes intense as well as the concentration of these aggregates is higher in thin films, moreover, the probability of exciton trapping in localized aggregates decreases as the temperature increases due to the *thermally activated hopping* process. All these features have been observed in film thicker 2 *nm*, in particular in sample grown at low deposition rate in which an high nucleation density of the three-dimensional aggregates has been found.

Lifetime measurements

Time-resolved fluorescence measurements were carried out in order to determine the effects of the exciton dynamics by the presence of aggregates in T4DIM thin films. As discussed in *Section 1*, optical excitations in conjugated molecules are strongly bound electron-hole pairs, which are called Frenkel excitons and are usually localized on a single conjugated unit. Once created, excitons tend to migrate toward the lower energy sites, (i.e. defect states or aggregates), by means of energy transfer. Because of the disorder of T4DIM in thin films such a migration is a random walk, which can be regarded as a diffusion process. In this direction, the exciton dynamics in thin films can be better understood if confronted with that of a well order structure in single crystal of T4DIM. The fluorescence decay of a single crystal at room temperature can be represented by a single exponential (*Figure 4.13)*, with a decay time τ of 0.73 *ns*. Whit respect to the crystalline material, the normalized fluorescence decays all T4DIM films, integrated over all wavelengths, can be fit using a biexponential function of the form : $F_{tot} = A e^{-k_A t} + B e^{-k_B t}$. All samples show temperature-dependent fluorescence decays and spectral shifting most likely

due to an energy transfer to lower energy levels. These variations in the fluorescence spectra and decays, moreover, are depending by the growth conditions of the thin films (*see Table 3*). In fact, with respect to the lifetime of the single crystal, a substantial decrease of the average lifetime was observed for the thin films grown at the higher deposition rate (0.1 *Å/s*). In these sample, moreover, as the thickness increases the long-time component of the fluorescence decays increases. At lower kinetics of growth (0.01 *Å/s*) the decay emission profile does not change so much with respect to that of the crystal, in particular for the sample of 5 *nm* of nominal thickness. For this sample, in a separate series of experiments, I measured the time- and wavelength-resolved luminescence at two temperatures 77 to 295 *K*, respectively, using streak camera detection in conjunction with a liquid nitrogen cryostat. As shows in *Figure 4.14* few hundred picoseconds after excitation a shifting and reshaping of the fluorescence spectrum were observed.
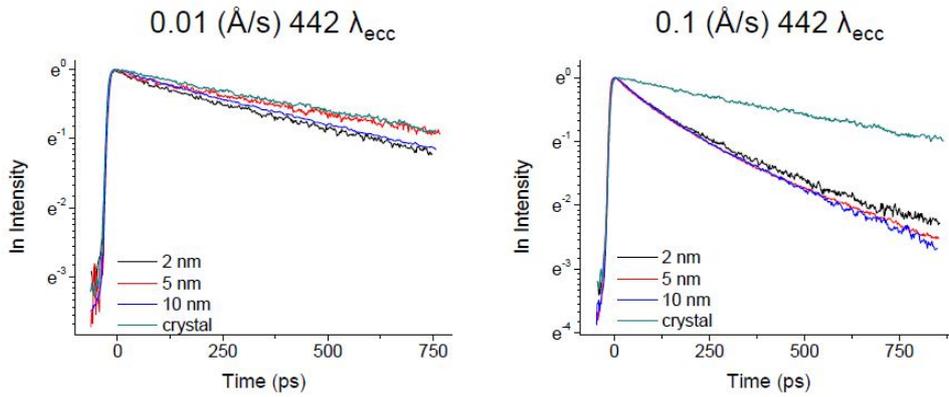
Figure 4.13 *Fluorescence decays profile of T4DIM thin films of 2,5,10 nm of nominal thickness. Kinetics of growth a) 0.01Å/s and b)0.1Å/s. (Wavelength excitation 442nm) .*

Sample	0.01 (Å/s)	0.01 (Å/s)
2 (*nm*)	$\tau_1 = 60$, $\tau_2 = 62$	$\tau_1 = 70$, $\tau_2 = 300$
5 (*nm*)	$\tau_1 = 30$, $\tau_2 = 728$	$\tau_1 = 96$, $\tau_2 = 345$
10 (*nm*)	$\tau_1 = 140$, $\tau_2 = 720$	$\tau_1 = 96$, $\tau_2 = 355$
crystal	$\tau = 735$	

Table 3. *Lifetime values for the corresponding emission decay profile shown in figure 15*

These results are in agreement with an energy transfer process that is temperature dependent. In fact, at room temperature this process is faster with respect to the lower temperature (*Figure 4.14a* and 4.14*b*). As discuss in steady state investigation

at room temperature regime, the exciton diffusion consists of two steps, namely the downhill migration and the thermally activated hopping, while at lower temperatures the downhill migration fully determines the diffusion process. Thus the two mechanisms are characterized by a different exciton diffusion length. In particular, as the temperature increases the diffusion length is high respect to that at low temperature. As consequence the probability of transferring energy from an excitonic level to an aggregates increase. In order to analyze this data, I require a model for the excited state that takes into account contributions from at least two different emitting species within the thin film. The simplest possible model to describe the fluorescence decay dynamics is outlined in *Figure 4.15* State 1 corresponds to the exciton that emits at early times, while state 2 corresponds to a lower energy level whose emission grows in at later times. The states decay to the ground state with rates $kr1$ and $kr2$, and population can also be transferred from state 1 to state 2 with rate Γ. The assumption that only two distinct species, contributed to the fluorescence is probably an oversimplification, nevertheless the validity of model is support by experimental data. The next question concerns the identity of states 1 and 2. The simplest assumption would be that state 2 arises from a two-dimensional 3D aggregate like the one pictured in *Figure 4.10b*, which is intrinsic to the ideal structure of the T4DIM crystal.
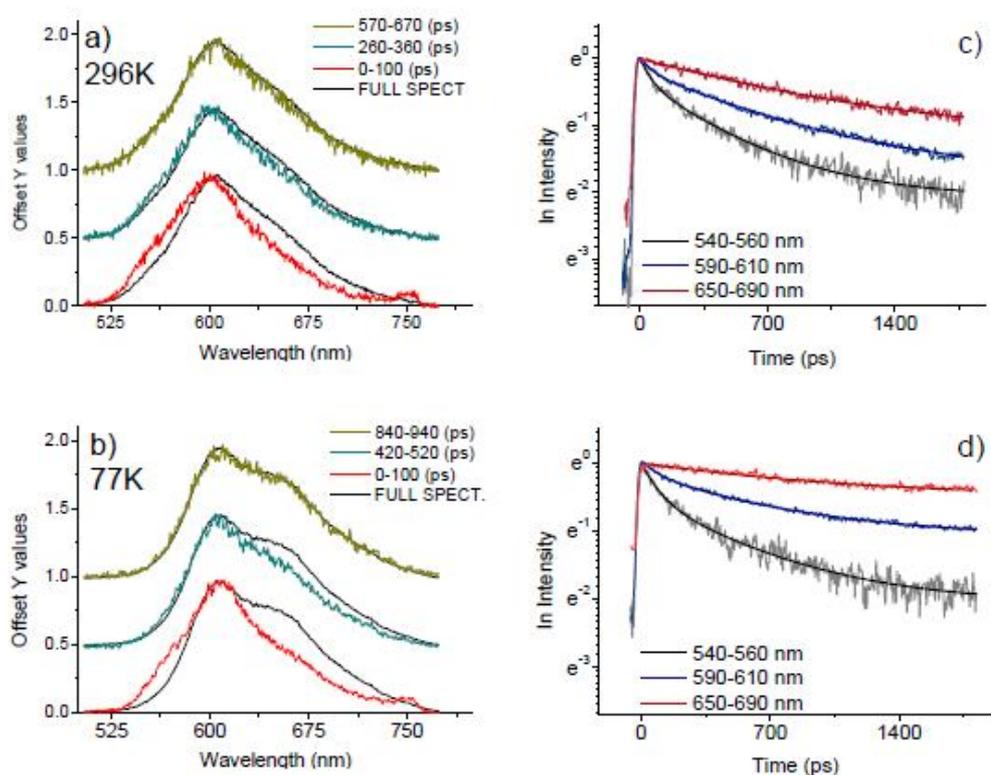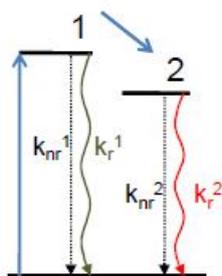
Figure 4.15 *Level diagram for analysis of the experimental data. Level 1 corresponds to the intrinsic exciton, whereas level 2 represents lower energy defect states.*

4.4 Optoelectronic performance of T4DIM in single layer transistor

In the previous sections we have reported on how the optical properties in T4DIM molecular thin films are deeply affected by different factors such as the nature of substrates and the kinetic of the growth process. Indeed, these factors causes the molecules to form aggregates whit different molecular packing motifs with respect the well-ordered crystalline material. It is evident that the aggregates that we have identified by means of the morphological and photophysical investigation can in turn play a role in determining the charge transport properties in thin-films. Given that T4DIM has been recently introduced as a highly performing active material in single-layer OLETs, we try to correlate the optoelectronic performances of two OLETs devices fabricated by sublimation of T4DIM at the same deposition rates conditions (0.1 and 0.01 *Å/s*) we have used in the mirco-spectroscopic characterization we have performed. Moreover, it is well-known that OLETs can be considered as truly "interface" devices given that charge-transport and light-formation process take place at the first monolayers at the interface with the dielectric layer.
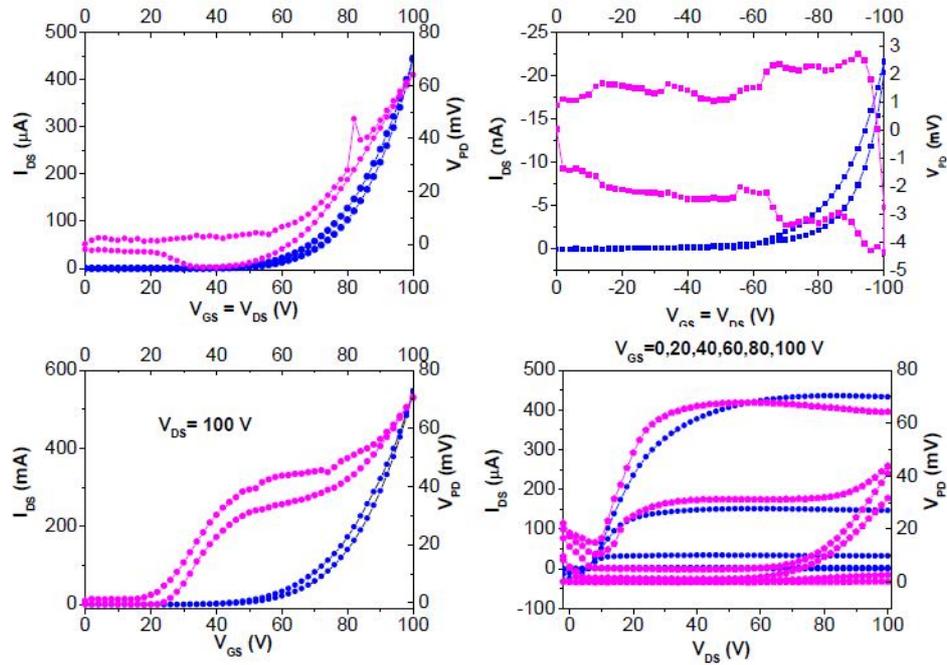
Figure 4.16. *Electrical characteristics, (blue) and corresponding light emission intensity (purple) of single layer OFET based on T4DIMgrown at 0.01 Å/s. (a, b) n type (a) and p-type (b) locus curves. (c) n-type transfer saturation curve, and (d) n-type multiple output curves*

The devices were fabricated in bottom-gate/top-contact configuration with a 30 nm-thick active layer, give that this configuration showed the best optoelectronic performances. The optoelctronic characteristics are reported in *Figure 4.16* and *Figure 4.17* for the *0.01* and *0.1 Å/s* deposition rate conditions respectively. Both OLET devices display an ambipolar charge transport and light-emission. In particular, for the device in which T4DIM is grown at the lower deposition rate, charge transport is overwhelmed by electrons as the high value of the *n*-type mobility demonstrates ($\mu_N = 0.48 \ cm^2/ \ Vs$, $V_{TN} = 57 \ V$) (*Figure 4.16a*). A three-order-of-magnitude lower hole mobility ($\mu_P = 1.9 \cdot 10^{-5} \ cm^2/ \ Vs$, $V_{TP} = -74 \ V$) is calculated from the n-type locus curve reported in *Figure 4.16b*. Light emission signal in the transfer characteristic is peaked in the ambipolar working region of the device, in agreement with the typical behavior reported for well-balanced ambipolar single layer OLET[17]. The electrical characterization for the device made with the higher sublimation rate is shown in *Figure 4.17*.
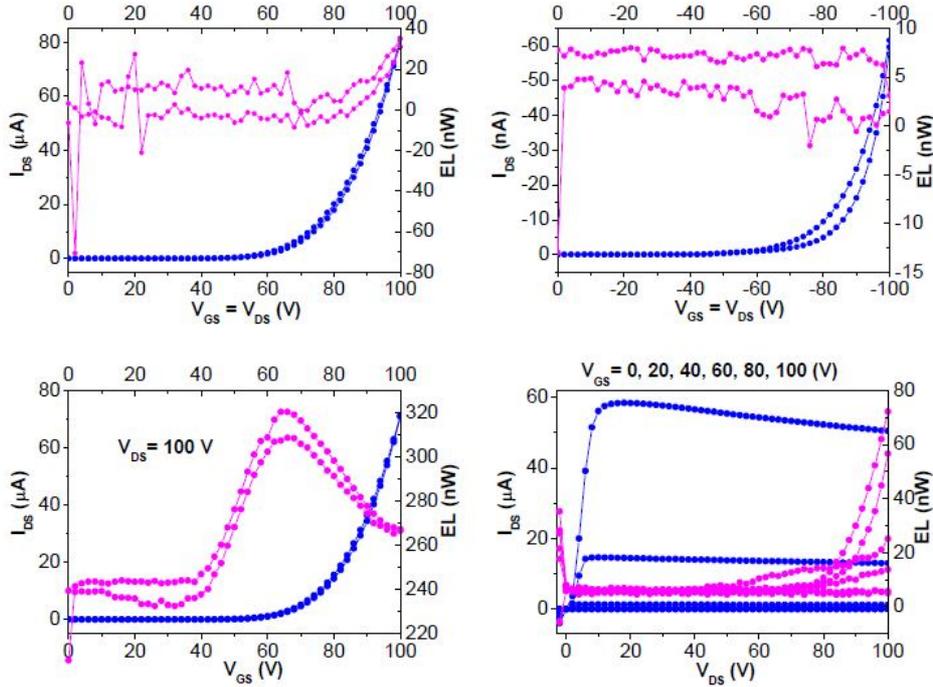
Figure 19. *Electrical characteristics (blue) and corresponding light emission intensity (purple) of single layer OLET based on T4DIM.grown at 0.1 Å/s (a, b) n type (a) and p-type (b) locus curves. (c) n-type transfer saturation curve, and (d) n-type multiple output curves*

Indeed, it can be observed that in this case the electron mobility is decreased by an order of magnitude, while the corresponding threshold voltage is not changed (0.053 cm^2/ Vs, $V_{TN} = 60$ $V)$. Moreover, in both type of devices the hole mobility ($\mu_P = 6.4 \cdot 10^{-5}$ cm^2/ Vs, $V_{TP} = -71$ V) is almost unaltered. Even though the evident unbalanced charge transport, the improvement of the electron transport features plays a major role in the generation of the electroluminescence signal clearly visible in the transfer saturation *n*-type and multiple output *n*-type curves reported in *Figure 4.16c and d*, respectively. (Please note that the different units used in the saturation transfer characteristics does not invalidate this statement).Moreover, the low-deposition rate T4DIM OLETs shows an optical power comparable to that of state-of-the-art single layer polymeric OLET devices. Even though further investigation is necessary and on-working, we believe that in the case of T4DIM OLETs an unambiguous correlation between the aggregate formation in the first monolayers of the thin-films and the modulation of the electronic transport and optical properties, as the optoelectronic performances of test devices show. It is evident that the study of the photophysics at the micrometric scale is a fundamental tools for investigating and optimizing light-formation and charge-transport processes in real-working optoelectronic devices.

References

[99] Koren, A. B.; Curtis, M. D.; Francis, A. H.; Kampf, J. W. *J. Am. Chem. Soc.* **2003**, 125, 5040–5050.

[100] Curtis, M. D.; Cao, J.; Kampf, J. W. *J. Am. Chem. Soc.* **2004**, 126, 4318–4328.

[101] Birks, J. B. *Photophysics of Aromatic Molecules*;Wiley: London, **1970**.

[102] Hong, Y.; Lama, J. W. Y.; Tang, B. Z. Aggregation-Induced Emission: Phenomenon, Mechanism and Applications. *Chem. Commun.* **2009**, 4332–4353.

[103] (a) Y. Yamashita, *Adv. Mater.*, **2009**, 10, 024313; (b) S. Allard, M. Forster, B. Souharce, H. Thiem and U. Scherf, *Angew. Chem.*, **2008**, 120, 4138; (c) H. Sirringhaus, *Adv. Mater.*, **2005**, 17, 2411.

[104] (a) A. Mishra, C.-Q. Ma and P. Ba¨ uerle, *Chem. Rev.*, **2009**, 109, 1141; (b) G. Barbarella, M. Melucci and G. Sotgiu, *Adv. Mater.*, **2005**, 17, 1581.

[105]L. Pauling, *The nature of the chemical bond*, Cornell University, Ithaca, NY, **1945**.

[106] M. Muccini et al. *Adv. Mater.* **2001**, 13, 355-358

[107] M. A. Loi, E. Da Como, F. Dinelli, M. Murgia, R. Zamboni, F. Biscarini and M. Muccini*, Nature Materilas,* vol 4, **2005,** 81- 85

[108]D. Oelkrug, A. Tompert, J. Gierschner, H. J. Egelhaaf, M. Hanack, M. Hohloch, and E. Steinhuber, "Tuning of fluorescence in films and nanoparticles of oligophenylenevinylenes," *J. Phys. Chem. B*, vol. 102, pp. 1902–1907, **1998**.

[109] R. Resel, N. Koch, F.Meghdadi, G. Leising, L.Athouel, G.Froyer, F.Hofer, *Cryst. Res. Technol.* **2001**, 36, 47

[110] Movaghar, B.; Gru¨newald, M.; Ries, B.; Ba¨ssler, H.; Wu¨rtz, D. *Phys. Rev. B* **1986**, *33*, 5545–5554.

[111] Wantz, G.; Hirsch, L.; Dautel, O. J. *Appl. Phys. Lett.* **2007**, *90*, 162104

[112] Oura, K.; V.G. Lifshits, A.A. Saranin, A.V. Zotov, and M. Katayama (**2003**). *Surface Science: An Introduction.* Berlin: Springer

[113] O. V. Mikhnenko, F. Cordella, A. B. Sieval, J. C. Hummelen, P. W. M. Blom, and M. A. Loi, *J. Phys. Chem. B* **2008**, *112,* 11601–11604

[114] R. Capelli, S. Toffanin, G. Generali, H. Usta, A. Facchetti and M. Muccini, *Nat. Mater.*, **2010**, 9, 496C.

Chapter 5

Conclusion and Perspective

The work presented in this PhD thesis aims at describing the solution and solid-state photophysical properties of a novel ambipolar semiconductor (T4DIM) in order to investigate the intimate connection between molecule chemical structure, the thin-film molecular arrangement and the overall optoelectronic performances of the organic multifunctional devices.

In particular, the description of the solid state electronic properties of organic materials necessitates of taking into account the nature of intermolecular interactions which depends, among others, on the molecular arrangement in the solid state. In the technologically appealing thin films, the molecular arrangement is extremely sensitive to the deposition procedures and to the nature of the substrate.

Thus, of great interest is the understanding at the micro- and nano-scale of the molecular architecture and morphological features which favor charge transport and/or energy transfer, in order to enhance performances of opto-electronic devices based on thin films. Whereas it has been demonstrated that the molecular properties can be tuned by chemical tailoring, morphology and supramolecular arrangement are generally more difficult to control, and this appears to be one of the next challenges in the field of organic π-conjugated materials.

Firstly, we have started investigating the optical problem of T4DIM in solution, in particular by performing a solvent-dependent study for probing the molecular photophysical processes. Indeed, with increasing the solvent polarity a bathocromical shift in the fluorescence spectra together with a decrease of the quantum yield is observed. We have demonstrated that in this compound an internal charge transfer (ICT) occurs in excited state. In fact, the intensity modulation the fluorescence due

the solvent polarity is a clear evidence of a charge transfer from the strong electron-withdrawing thieno(bis)imide (TBI) moieties, towards the electron-donating thiophene core. Time-resolved fluorescence measurements confirms that in low-polarity solvents T4DIM emits at short wavelengths from the local excited (LE) state while in high-polar solvent a longer-wavelength emission comes from an ICT state, which forms rapidly after excitation. Thus, the insertion of TBI moieties as oligothiophene end is directly correlated to the appearance of intramolecular charge transfer mechanism which in turn can be possibly connected to the ambipolar charge transport and electroluminescence performed by the molecule in solid-state. As we have previously discussed , electronic and optical properties in small-molecule organic thin-films are very sensitive to sample growth conditions and the nature of the substrate Indeed, we performed low-temperature time-resolved photoluminescence spectroscopy cross-correlated with morphological investigation on T4DIM in thin-films in order to understand how variations in the molecular packing motif and in the supramolecular arrangement can be interconnected with exciton and charge carrier dynamics at the nanoscale.

In particular, we have demonstrated that the self organization of T4DIM molecules are dependent on the surface energy of the substrate (in particular dielectric) and on the growth kinetics during the sublimation process. By means of AFM investigation it is proved that at the early stage of growth on suitable substrates the structural topology of T4DIM films are dominated by the presence of molecular aggregates. The crystalline nature and the concentration of the aggregates can be evidenced by the spectral modulation of the photoluminescence spectra, especially at low temperature.

Time resolved photoluminescence spectroscopy performed throughout all the samples has reveled that the excitation energy is transferred from the excitonic band to lower energy state a few hundred picoseconds after excitation.

We have discussed these result in the framework of excitonic dynamics, in particular referring to exciton downhill migration together with spectral diffusion.

In order to correlate the microscopic overview of the photophysical processes in T4DIM thin-films with optoelectronic performances of multifunctional devices, we fabricated single-layer organic light-emitting transistors implementing T4DIM as active material. Given that they are considered as *true interface* device, organic field-effect transistor are an ideal platform for investigating light-formation and charge

transport processes taking place at the first monolayers from the dielectric surface. Indeed, an improvement of the external quantum efficiency is observed for the devices fabricated in the specific growth conditions (deposition rate and dielectric layer) for which the formation of well monodisperse crystalline aggregates is expected in monolayer samples.

Thus, we can infer that in the case of T4DIM the specific supramolecuar arrangement motif can play a fundamental role in determining the macroscopic overall device performances. It is evident that the comprehension of the intimate nature of the aggregates (crystalline vs amorphous) together with a detailed investigation of the exitonic and electronic processes (enery/charge transfer, charge diffusion, charge trapping…) is an essential tool for guiding the optimization of optoelectronic organic devices.

Acknowledgements

I would like to thank all the people who supported me during this PhD work and encouraged me to give always the best from myself.

In particular I would like to thank my University supervisor, Prof *Giorgio Orlandi* and my CNR-ISMN supervisors Dr. *Michele Muccini* and Dr. *Stefano Toffanin*.

A warm thank also to all my colleagues from CNR of Bologna, *Raffaella Capelli*, *Viviana Biondo*, *Gialuca Generali*, specially to *Wouter Koopman* who accompanied me in this journey.

Publications List

● *Thienopyrrolyl dione end-capped oligothiophene ambipolar semiconductors for thin film- and light emitting transistors.*
Author(s): M.Melucci, M. Zambianchi, L. Favaretto, M. Gazzano, A. Zanelli, M. Monari, R Capelli, S. Troisi, S. Toffanin and M. Muccini, *Chem. Commun.*, **2011**, **47**, *11840–11842*

● *Molecular tailoring of new thieno(bis)imide-based semiconductors for single layer ambipolar light emitting transistors.*

Author(s): M. Melucci, L. Favaretto, M. Zambianchi, M. Durso, M. Gazzano, R. Capelli, M. Muccini, V. Biondo, S. Toffanin, S. Troisi,W. Koopman, F. De Angelis, M. Lobello, A. Zanelli, M. Monari, G. Generali, *Chemistry of Materials*

General. *2,3-dibromothiophene* **2**, and *bis(pinacoato)diboron* **8** were purchased from Alfa Aesar (Karlsuhe, Germany), *2-tributylstannylthiophene* **5** was purchased from Sigma-Aldrich (Taufkirchen, Germany), *5,5'-bis(tributylstannyl)-2,2'-bithiophene* **13** was prepared according to already reported procedures. All ^{1}H and ^{13}C NMR spectra were recorded with a Varian Mercury 400 spectrometer operating at 400 MHz (^{1}H). Chemical shifts were calibrated using the internal CDCl$_3$, acetone-d_6 or CD$_2$Cl$_2$ resonance which were referenced to TMS. Mass spectra were collected on a ion trap Finningan Mat GCQ spectrometer operating in electron impact (EI) ionization mode. Each sample was introduced to the ion source region of GCQ via a direct exposure probe (DEP). The melting points were determined by a Bùchi 510 apparatus.

3-Bromothiophene-2-carboxylic acid, **9** [yield: 89%; white powder].
M.p. 191°C, MS (70 eV, EI): m/z 208 (M$^{\cdot +1}$),^{1}H NMR (acetone-d$_6$, TMS/ppm) δ 7.85 (d, ^3J=5.2 Hz, 1H), 7.22 (d, ^3J=5.2 Hz, 1H). ^{13}C NMR (acetone-d$_6$, TMS/ppm) δ 162.6, 134.6, 133.8, 129.9, 117.6

Thiophene-2,3-dicarboxylic acid, **10** [yield: 89%; white powder]. MS (70 eV, EI): m/z 172 (M$^{\cdot +1}$); ^{1}H NMR (acetone-d$_6$, TMS/ppm) δ 7.89 (d, ^3J=5.2 Hz, 1H), 7.71 (d, ^3J=5.2 Hz, 1H). ^{13}C NMR (acetone-d$_6$, TMS/ppm) δ 167.4, 163.8, 135.6, 134.4, 133.8, 133.5.

Thiophene-2,3-dicarboxylic anhydride, **11** [yield: 78%; pale yellow crystals]. M.p. 147.5°C, MS (70 eV, EI): m/z 155 (M$^{\cdot +1}$), ^{1}H NMR (acetone-d$_6$, TMS/ppm) δ 8.42 (d, ^3J=4.8 Hz, 1H), 7.57 (d, ^3J=4.8 Hz, 1H). ^{13}C NMR (acetone-d$_6$, TMS/ppm) δ 159.5, 158.7, 147.4, 145.4, 143.2, 123.3.

3-Butylcarbamoylthiophene-2-carboxylic acid, **12** and *2-butylcarbamoylthiophene-3-carboxylic acid,* **12'** MS (70 eV, EI): m/z 227 (M$^{\cdot -1}$), ^{1}H NMR (CDCl$_3$, TMS/ppm) δ majority isomer 7.58 (d, ^3J=5.6 Hz, 1H), 7.30 (d, ^3J=5.6 Hz, 1H), 6.61 (broad s, 1H), 3.50 (m, 2H), 1.65 (m, 2H), 1.42 (m, 2H), 0.98 (t, 3H). ^{13}C NMR (CDCl$_3$, TMS/ppm) δ majority isomer 164.9, 161.8, 134.7, 131.5, 126.6, 126.5, 40.5, 31.1, 20.1, 13.7.

5-Butylthieno[3,2-c]pyrrole-4,6-dione, **3:** [yield: 99%; dark yellow oil]. MS (70 eV, EI): m/z 209 (M$^{.+1}$), ^{1}H NMR (CDCl$_3$, TMS/ppm): δ ≡ 7.74 (d, 1 H, J = 4.8 Hz), 7.27 (d, 1 H, J = 5.2 Hz), 3.57 (t, 2H), 1.59 (m, 2H), 1.33 (m, 2H), 0.91 (t, 3H). ^{13}C NMR (CDCl$_3$, TMS/ppm) δ ≡ 163.8, 162.7, 144.6, 140.7, 137.2, 120.9, 38.1, 30.7, 19.9, 13.5.*2-Bromo-5-butyl-5H-thieno[3,2-c]pyrrole-4,6-dione,* **4**: [yield: 78%; off-white solid]. M.p. 61 °C; MS (70 eV, EI): m/z 289 (M$^{.+1}$); ^{1}H NMR (CDCl$_3$, TMS/ppm) δ ≡ 7.29 (s, 1 H), 3.57 (t, 4 H), 1.6 (m, 24H), 1.33 (m, 4H), 0.92 (t, 3H). ^{13}C NMR (CDCl$_3$, TMS/ppm) δ 162.9, 161.9, 143.8, 140.4, 125.3, 123.7, 38.3, 30.7, 19.9, 13.6.

5-Butyl-2-(thiophene-2-yl)-5H-thieno[3,2-c]pyrrole-4,6-dione, **6**: [yield: 75%; bright yellow microcrystals]. M.p. 143°C, MS (70 eV, EI): m/z 291 (M$^{.+1}$), ^{1}H NMR (CDCl$_3$, TMS/ppm) δ 7.38 (dd, ^3J=5.2 Hz, ^4J=1.2 Hz, 1H), 7.32 (dd, ^3J=3.6 Hz, ^4J=1.2 Hz, 1H), 7.31 (s, 1H), 7.08 (dd, ^3J=5.2 Hz, ^3J=3.6 Hz, 1H), 3.60 (t, 2H), 1.63 (m, 2H), 1.36 (m, 2H), 0.94 (t, 3H). ^{13}C NMR (CDCl$_3$, TMS/ppm) δ 164.0, 162.9, 145.1, 143.3, 137.4, 135.2, 128.3, 127.2, 126.1, 116.6, 38.3, 30.8, 20.0, 13.6.

2-(5-Bromothiophen-2-yl)-5-butyl-5H-thieno[3,2-c]pyrrole-4,6-dione, **7:** [yield: 99%; bright yellow solid]. M.p. 170°C, MS (70 eV, EI): m/z 370 (M$^{.+1}$), ^{1}H NMR (CDCl$_3$, TMS/ppm) δ 7.24 (s, 1H), 7.07 (d, ^3J=3.6 Hz, 1H), 7.04 (d, ^3J=3.6 Hz, 1H), 3.60 (t, 2H), 1.62 (m, 2H), 1.35 (m, 2H), 0.94 (t, 3H). ^{13}C NMR (CDCl$_3$, TMS/ppm) δ 163.8, 162.7, 148.8, 145.1, 137.8, 136.5, 131.1, 126.2, 116.8, 114.4, 38.3, 30.8, 20.0, 13.6.

2,2'-(2,2'-Bithiophene-5,5'-diyl)bis(5-butyl-5H-thieno[3,2-c]pyrrole-4,6-dione), **T4DIM** [yield: 75%; red powder] M.p. 277 °C, MS (70 eV, EI): m/z 580 (M$^{.+1}$); ^{1}H NMR (CD$_2$Cl$_2$, TMS/ppm) δ 7.36 (s, 2 H), 7.32 (d, ^3J=4.0 Hz, 2H), 7.04 (d, ^3J=4.0 Hz, 2H), 3.60 (t, 4H), 1.63 (m, 4H), 1.36 (m, 4H), 0.96 (t, 6H). Anal. Calcd for C$_{28}$H$_{24}$N$_2$O$_4$S$_4$ (580.76): C, 57.91; H, 4.17. Found: C, 57.99; H, 4.27.